Development of 3D-Printed Skin Suturable Models for Surgical Simulation

Abstract

The skin is a complex and dynamic organ that acts as a physical and immunological barrier while contributing to thermoregulation, sensory perception, and vitamin D synthesis. Because of its multilayered structure and the regional variability of its mechanical and anatomical properties, skin remains difficult to replicate using advanced three-dimensional printing technologies, including Stratasys Digital Anatomy®™ printers. Accurate reproduction of its anatomical and biomechanical characteristics is essential for the development of realistic models for clinical, surgical, and educational applications.

This study investigates photopolymer material blends for the fabrication of three-dimensional printed skin models, with particular emphasis on their ability to simulate cutting and suturing in clinically relevant regions such as the temporal area and the abdomen. A literature review was first conducted to identify the main structural and mechanical properties of human skin and to guide model design. An experimental campaign was then performed to characterize skin behavior during the surgical actions of interest and to evaluate and refine the performance of the candidate materials. The testing protocol included tensile, puncture, cutting, suturing, and peeling tests, complemented by qualitative assessments performed with experienced surgeons to evaluate material usability.

More than 40 material combinations were examined, of which four were identified as the most representative. These were assigned to specific anatomical regions and further differentiated by age group. Finally, two demonstrative case studies are presented to validate the practical applicability of the proposed materials.

Keywords: Additive Manufacturing; 3D Printing; Skin; Surgical Training; Medical Education; Anatomical Modeling.

1. Skin structure

The skin is the largest organ of the human body, with an average surface area of approximately 2 m². It performs essential functions, including protection against external agents, thermal regulation, sensory perception, excretion of substances through sweating, and immune support [1]. From an anatomical perspective, the skin is organized into three main layers: the epidermis, dermis, and hypodermis (or subcutaneous tissue), each with specific histological and functional properties (Figure 1).

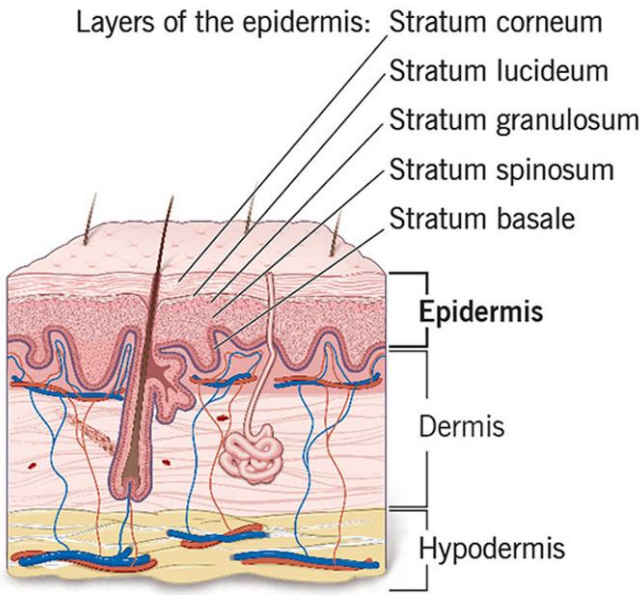


Figure 1: Layers of the skin *[2]*

The **epidermis** is the outermost layer and is composed of stratified keratinized epithelium. It contains five cellular layers: the basal, spinous, granular, lucid, and corneal (Stratum Corneum - SC) layers, the latter consisting of dead keratinized cells that form a physical barrier against water loss and environmental aggressions. The excretory ducts of sweat and sebaceous glands pass through the epidermis, although the glands themselves are in the dermis [1].

The **dermis** lies beneath the epidermis and consists of loose and dense connective tissue, rich in collagen and elastic fibers embedded in a hydrated extracellular matrix containing hyaluronic acid. It hosts a capillary vascular network, nerve endings, immune cells, and specialized sensory structures. The resident cells of the dermis, particularly fibroblasts, are responsible for the synthesis of structural proteins and components of the extracellular matrix. The maintenance of structural integrity and dermal hydration depends on the

production of these components, which tends to decrease with aging, contributing to the loss of elasticity and the formation of wrinkles [1].

The **hypodermis**, or subcutaneous layer, is the deepest component of the skin and contains a high concentration of adipose tissue, which functions as thermal insulation, mechanical cushioning, and a secondary energy reserve. It is traversed by blood vessels of larger caliber than those in the dermis and plays an active role in thermoregulation: in response to environmental temperature changes, vasoconstriction or vasodilation of these vessels modulate skin blood flow, thereby influencing heat exchange with the external environment [1].

Precise characterization of the composition and thickness of each of these layers is essential for the accurate reproduction of skin in 3D-printed anatomical models, particularly in surgical or biomechanical simulation contexts. In the literature, the most used techniques for measuring skin thickness include Optical Coherence Tomography (OCT), Laser Scanning Microscopy (LSM), and histological analysis, all of which provide highly consistent results. Ultrasound (US), although widely employed for dermal assessment [3], tends to overestimate the thickness of the epidermis and must therefore be used with caution when characterizing the most superficial layer [4].

Numerous studies have examined the factors influencing skin thickness, identifying anatomical location and subject age as the main determinants. The literature has also considered sex, ethnicity, chronic sun exposure, and smoking habits; however, no statistically significant correlations have been found between these latter factors and variations in skin thickness [4] [5].

Based on the collected data [3] [4] [5] [6] [7] a statistical analysis of the average thickness values of the skin layers was conducted. The results of this analysis are presented in the following summary tables, which include an overview of average values, a breakdown by age group, and a comparison across different anatomical regions.

Table 1: Mean skin thickness and standard deviation (SD, in parentheses) reported for each cited study. The number of samples considered in each study is also indicated. A final row reports the overall mean value of the sum of the three layers.

Reference	# of samples	Skin layer	Mean value (SD) [µm]
Tsugita-2013 [7]	1044	Stratum Corneum	13.85 (0.98)
Lintzeri-2022 [4]	1697	Epidermis	72.3 (10.18)
Lee-2002 [6] Firooz-2016 [3]	150	Dermis	1279.21 (295.15)

		Total thickness	**1365.36**

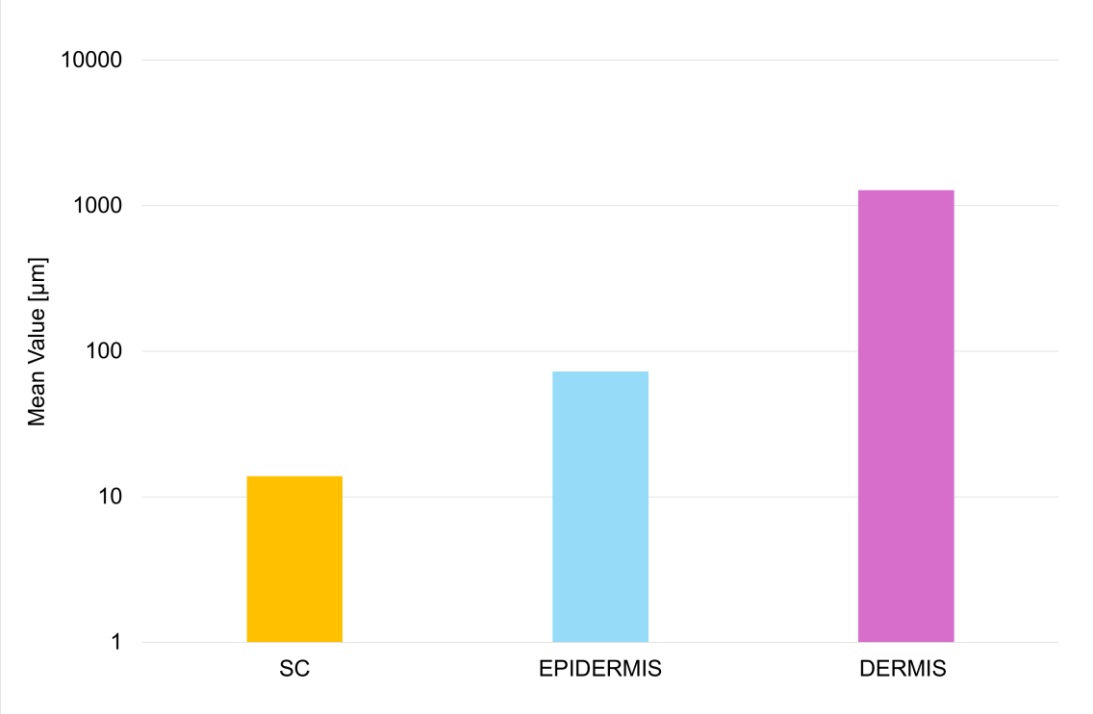


Figure 2: Histogram showing the mean thickness of the different skin layers: Stratum Corneum (SC), Epidermis and Dermis

Table 2: Mean thickness values and standard deviation (SD, in parentheses) reported in the literature for each of the skin layers considered, divided by age group.

Reference	# of samples	Age range	Skin layer	Mean value (SD) [µm]
Tsugita-2013 [7]	522	<35	Stratum Corneum	13.95 (0.97)
	522	≥ 35		13.74 (1.03)
Lintzeri-2022 [4]	764	<35	Epidermis	80.68 (5.41)
	933	≥ 35		65.18 (7.49)
Firooz-2016 [3]	75	<35	Dermis	1416.84 (182.12)
	75	≥ 35		1310.03 (231.56)

<35	**Total thickness**	**1511.47**
≥ 35		**1388.95**

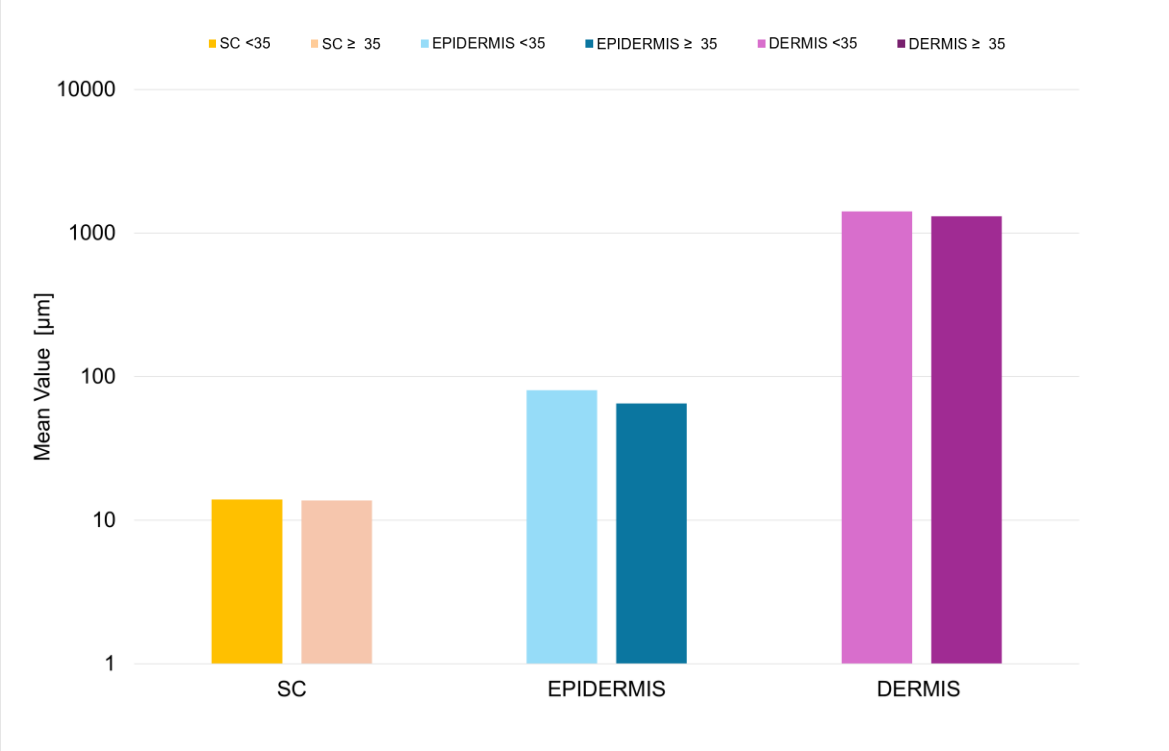


Figure 3: Histogram of the mean thickness values for each of the skin layers considered, divided by age groups: <35 and ≥35.

Table 3 presents summary statistics for the mean thickness values of the different skin layers, stratified by anatomical group and age range. Firooz et al. (2016) [3] used US to

estimate dermal thickness in specific anatomical regions, such as Head & Neck, Palm, Sole, and Dorsum of foot. Accordingly, these values may be overestimated.

Table 3: Average thickness values of the individual skin layers are grouped by age range. For each value, the number of reference samples on which statistics (mean values and SD) are computed is reported.

Reference	# of samples	Group	Skin layer	Age range	Mean value (SD) [µm]
Tsugita-2013 [7]	116	GROUP 1 - HEAD & NECK	Stratum Corneum	<35	14.71 (1.15)
	116			≥ 35	14.91 (0.16)
Lintzeri-2022 [4]	173		Epidermis	<35	76.55 (8.84)
	197			≥ 35	56.85 (8.27)
Firooz-2016 [3]	30		Dermis	<35	1549.76 (138.36)
	30			≥ 35	1490.00 (199.31)
Tsugita-2013 [7]	58	GROUP 2 - BACK	Stratum Corneum	<35	14.73 (1.35)
	58			≥ 35	14.33 (1.46)
Lintzeri-2022 [4]	58		Epidermis	<35	78.10 (6.23)
	69			≥ 35	71.80 (5.03)
Tsugita-2013 [7]	174	GROUP 3 - ARM	Stratum Corneum	<35	13.76 (0.69)
	174			≥ 35	13.51 (0.84)
Lintzeri-2022 [4]	256		Epidermis	<35	82.87 (5.75)
	336			≥ 35	69.63 (6.80)
Tsugita-2013 [7]	58	GROUP 4 - ABDOMEN	Stratum Corneum	<35	14.61 (1.55)
	58			≥ 35	14.15 (1.67)
Lintzeri-2022 [4]	73		Epidermis	<35	83.00 (5.05)
	56			≥ 35	60.70 (10.76)
Tsugita-2013 [7]	116	GROUP 5 - LEG	Stratum Corneum	<35	12.77 (0.44)
	116			≥ 35	12.44 (0.52)

Lintzeri-2022 [4]	185		Epidermis	<35	81.33 (5.34)
	275			≥ 35	65.57 (6.37)
Firooz-2016 [3]	15	PALM	Dermis	<35	1147.67 (228.47)
	15			≥ 35	1056.00 (190.64)
Firooz-2016 [3]	15	SOLE	Dermis	<35	1365.00 (261.60)
	15			≥ 35	1115.93 (179.66)
Firooz-2016 [3]	15	DORSUM OF FOOT	Dermis	<35	1472.00 (549.21)
	15			≥ 35	1398.20 (341.72)



Figure 4: Statistics were performed by dividing the data according to anatomical group and skin layer (the thickness values for palm, sole, and dorsum of the foot were combined by calculating the mean value). For some anatomical groups, the dermis is not represented, as the reference literature does not report an age-specific distinction.

The overall analysis of the data presented in the tables and graphs demonstrates a clear correlation between skin-layer thickness and the age of the subjects. A progressive decrease in total skin thickness is observed with increasing age, a trend consistently identified across all anatomical regions considered. This pattern involves the epidermis, dermis, and stratum corneum and appears stable across the two age groups analyzed (<35 years and ≥35 years), suggesting a generalized age-related effect on skin structure.

A review of the literature further confirms that age is a primary determinant of skin thickness, followed by anatomical location. For simulation purposes and based on published evidence as well as interviews with senior clinicians from relevant specialties, we elected to focus the characterization of tissue properties on three main anatomical macro-areas: (1) head and neck, (2) abdomen, and (3) back, arms, and legs.

Below, we provide additional details regarding the head and neck and abdominal regions, as these exhibit specific characteristics relevant to surgical simulation.

2. Site Specific Skin Structure

2.1 Temporal Bone

In the temporal region, the tissues overlying the bone exhibit a well-defined layered structure, progressing from the bony plane to the external surface in the following order: temporalis muscle (TM), deep temporal fascia, loose areolar tissue, superficial temporal fascia, and skin.

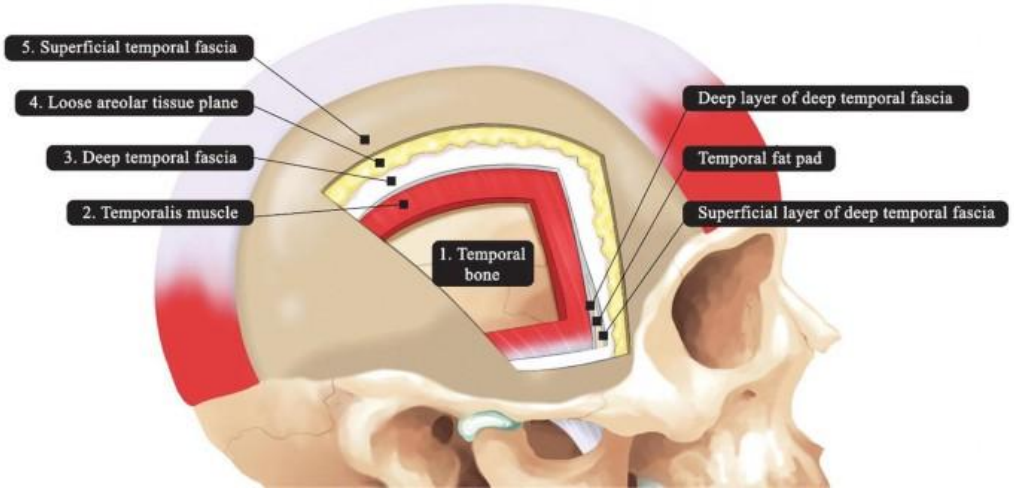


Figure 5: Temporal bone layers *[8]*

Regarding the epidermis, some studies have reported its thickness separately from the dermis, while others have considered the skin as a single entity (epidermis + dermis). The collected data show that epidermal thickness ranges from 0.042 mm (± 0.012) to 0.341 mm (± 0.153). The lowest values were observed in studies conducted on cadavers, where preservation and tissue preparation processes may affect the measurements. Dermal thickness, on the other hand, ranges from 1.049 mm to 1.245 mm. When including all

studies, also those evaluating total skin thickness (epidermis + dermis) the reported mean value is approximately 2.42 mm, with a standard deviation of about 1 mm.

Beneath the skin lies the subcutaneous adipose tissue (fat), which shows an average thickness of 2.95 mm. Deeper still is the temporal muscle, with an average thickness of approximately 5.43 mm [9] [10] [11] [12] [13] [14] [15].

Table 4: Mean thickness values and standard deviation (SD, in parentheses), reported in the literature for each of the skin layers considered. “Total Skin” refers to the sum of Epidermis and Dermis.

Reference	# samples	Layer	Mean value [mm]
Yildiz – 2020 [9] Chopra – 2015 [10] Jeong – 2023 [11] Kim – 2019 [13]	226	Total Skin	2.42 (1)
Kim – 2019 [13] Han – 2024 [15]	66	Fat	2.95 (1.39)
Gatto – 2024 [12] Han – 2024 [15] Uehata – 2017 [14]	326	TM	5.43 (1.20)

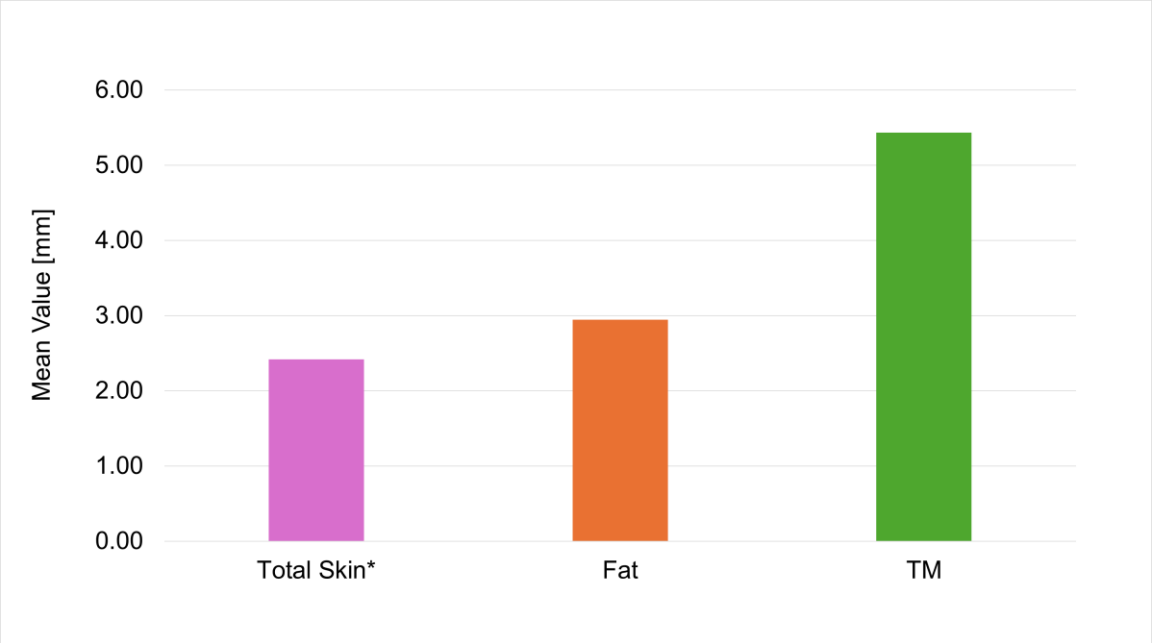


Figure 6: Histogram of the mean thickness of the skin layers considered. “Total Skin” refers to the sum of Epidermis and Dermis, while the “TM” refers to the temporalis muscle.

2.2 Abdomen

The anterior abdominal wall has a well-defined layered structure, as shown in Figure 7. Starting from the outside, the skin, composed of the epidermis and dermis, is followed by Camper's fascia, a superficial adipose layer of the abdominal subcutaneous tissue. Just beneath it lies Scarpa's fascia, a thin membranous layer that separates the superficial fat from the deep fat [16].

The deep fascia overlies the abdominal musculature, which is composed of three lateral muscle layers: the external oblique, internal oblique, and transversus abdominis. Medially, the rectus abdominis muscle is enclosed within the rectus sheath, formed by the aponeuroses of the lateral muscles [16].

Deeper layers of the abdominal wall include the transversalis fascia, extraperitoneal tissue, and finally the parietal peritoneum, which lines the abdominal cavity [16].

This stratification is essential for understanding the biomechanical behavior of the abdominal wall and is particularly relevant for surgical planning, such as trocar placement during laparoscopic procedures [16].

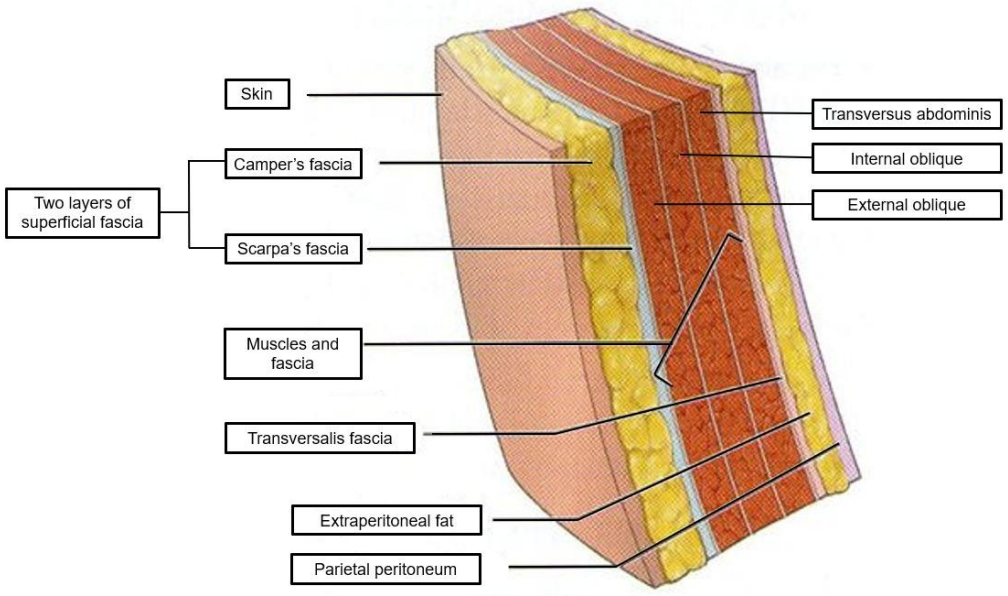


Figure 7: Anatomical layers of the anterior abdominal wall adapted from '*Anatomy of Anterior Abdominal Wall* by *Prajwal Rk* [Slide presentation]. Modified by the authors *[17]*.

The average thickness of the epidermis, evaluated across three studies using different methods, ranges from 0.06162 mm to 0.0801 mm, with an overall mean of approximately

0.074 mm. For the dermis, available data report values between 1.2484 mm and 1.95 mm, with a means of 1.6 mm.

Table 5: Mean thickness values, standard deviation (SD, in parentheses), and sample size reported in the literature for each of the abdominal layers. RA: Rectus Abdominus muscle, TA: Transversus Abdominus muscle, IO: Internal Oblique muscle, EO: External Oblique muscle.

Reference	# samples	Layer	Mean Value [mm]
Lintzeri – 2022 [4] Tsugita – 2013 [7] Lee – 2002 [6]	480	Epidermis	0.074 (0.02)
Lee – 2002 [6] Derraik - 2014 [18]	272	Dermis	1.599 (0.20)
Derraik - 2014 [18] Dong – 2015 [19] Rahmani – 2018 [22] Özdemir – 2025 [23]	363	Fatty layer	12.748 (3.90)
Abbas – 2022 [16] Tahan – 2016 [21]	388	RA	8.755 (2.13)
Abbas – 2022 [16] Tahan – 2016 [21] Rostami – 2013 [20] Rahmani – 2018 [22] Özdemir – 2025 [23]	478	TA	4.010 (0.99)
Abbas – 2022 [16] Tahan – 2016 [21] Rostami – 2013 [20] Rahmani – 2018 [22] Özdemir – 2025 [23]	478	IO	7.412 (1.41)
Abbas – 2022 [16] Tahan – 2016 [21] Rostami – 2013 [20] Rahmani – 2018 [22] Özdemir – 2025 [23]	478	EO	5.544 (1.18)

Regarding the adipose layers, the subcutaneous tissue shows an average thickness of approximately 12.75 mm, calculated from five studies employing CT and ultrasound techniques. The total muscular compartment has an average thickness of 6.43 mm, while the mean thickness values of individual abdominal muscles are as follows: rectus abdominis

(RA) 8.76 mm, transversus abdominis (TA) 4.01 mm, internal oblique (IO) 7.41 mm, and external oblique (EO) 5.54 mm.

These values, obtained from subjects of different age groups and using various measurement techniques, provide a useful quantitative reference for modelling the abdominal wall in biomechanical and surgical simulation contexts [16] [18] [19] [20] [21] [22] [23].

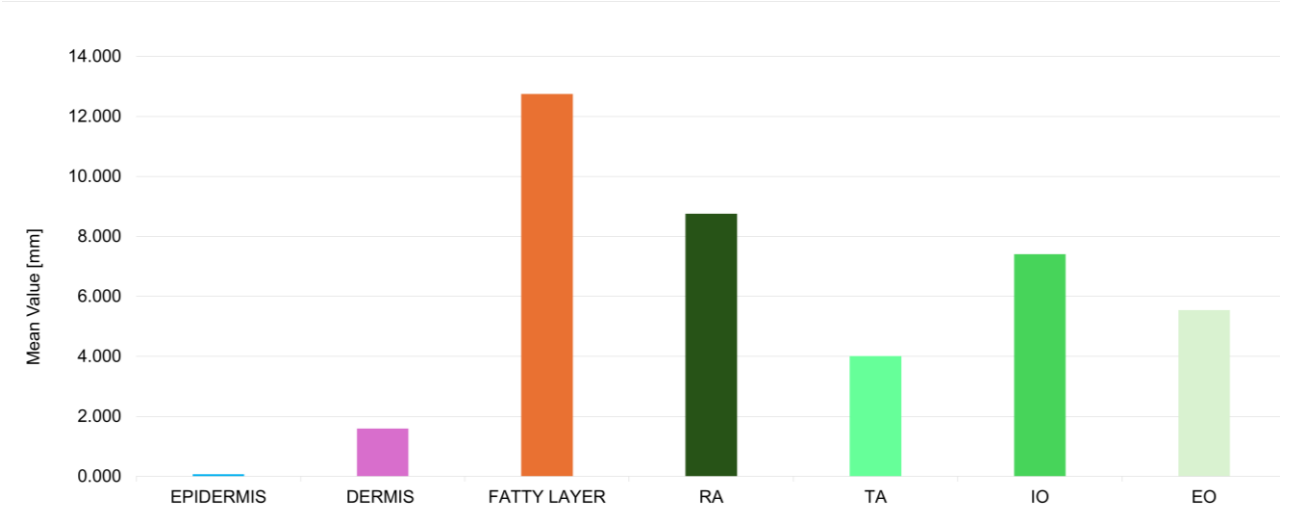


Figure 8: Histogram showing the average thickness values of the different tissue layers composing the anterior abdominal wall. The green bars represent the muscle layers: the rectus abdominis (RA), transversus abdominis (TA), internal oblique (IO), and external oblique (EO).

3. Skin Mechanical Properties

3.1 Literature Data

In addition to morphological aspects, a proper understanding of skin behavior requires the analysis of its mechanical properties, which are essential for applications in biomechanics, numerical modeling, and surgical simulation. The literature includes numerous studies employing various experimental methodologies, both in-vitro and in-vivo, to evaluate the mechanical characteristics of the skin.

One of the most comprehensive and detailed studies in this field is by Ottenio et al. [24], who analyzed the mechanical properties of human skin through uniaxial tensile tests on samples excised from the backs of cadavers. The aim was to assess the influence of two key variables: the orientation of the samples relative to Langer's lines and the strain rate. The samples were subjected to a pre-load of 2 N for small samples and 1 N for long samples

and preconditioned with 10 tensile cycles at an amplitude of 0.5 mm and a frequency of 1 Hz prior to data acquisition. The main mechanical parameters — including Young's modulus (E), Ultimate Tensile Strength (UTS), stretch ratio at UTS, stretch ratio at failure and strain energy — were calculated by separately considering each strain rate (regardless of orientation), each orientation (regardless of strain rate), and finally every specific combination of strain rate and orientation. Table 6 reports the average values obtained for each combination of orientation and strain rate. Results referring only to individual strain rates or orientations are available in the original article [24].

Table 6: Mean values of the mechanical properties of human skin obtained through uniaxial tensile tests, for each combination of orientation relative to Langer's lines and strain rate, as reported by Ottenio et al [24]. Standard deviation (SD) is indicated in parentheses.

Reference	# Sample	Orientation	Strain rates [s^{-1}]	UTS [MPa]	Stretch ratio at UTS	Stretch ratio at failure	Strain Energy [MJ/m^3]	E_2 [MPa]
Ottenio – 2014 [24]	33	Parallel	0.06	20.9 (1.3)	1.3 (0.0)	1.5 (0.1)	6.5 (1.8)	108.1 (25.9)
			53	32.1 (1.5)	1.2 (0.0)	1.3 (0.0)	5.6 (1.5)	152.4 (22.1)
			167	30.9 (3.7)	1.2 (0.0)	1.3 (0.1)	9.2 (4.0)	221.9 (16.6)
		45°	0.06	16.4 (6.4)	1.3 (0.0)	1.4 (0.1)	3.4 (0.9)	83.9 (40.6)
			53	23.7 (5.4)	1.3 (0.0)	1.3 (0.1)	4.1 (1.2)	105.4 (33.4)
			167	26.3 (10.0)	1.3 (0.0)	1.5 (0.2)	8.3 (4.5)	166.2 (67.1)
		Perpendicular	0.06	10.4 (1.3)	1.4 (0.0)	1.5 (0.1)	3.4 (1.8)	35.7 (25.9)
			53	16.7 (1.5)	1.3 (0.0)	1.4 (0.0)	4.2 (1.5)	54.9 (22.1)
			167	19.7 (2.0)	1.3 (0.0)	1.5 (0.1)	7.0 (4.0)	121.2 (16.6)

Samples oriented parallel to Langer's lines showed, on average, higher UTS values compared to those oriented perpendicularly, regardless of the applied strain rate. This trend was consistently observed at all three tested speeds, confirming the directional dependence of the skin's mechanical properties. Similarly, an increase in UTS was recorded with an increasing strain rate for all three orientations. This behavior suggests a viscoelastic response to the tissue, which becomes more resistant when stressed more rapidly. A similar trend was observed for the E_2 modulus, which represents the stiffness of the skin during the phase where collagen fibers are fully aligned. Here too, E_2 was influenced by both variables: samples aligned parallel to Langer's lines tended to exhibit significantly higher values compared to perpendicular samples, at the same strain rate. Furthermore, increasing the loading rate resulted in higher stiffness for all orientations. Regarding the stretch ratio at failure, a slight reduction in elongation was observed in parallel samples as the strain rate increased (from 1.5 to 1.3). For oblique (45°) and perpendicular orientations, no significant variation was detected. However, the authors note that this observation should be interpreted with caution due to the large standard deviations associated with these measurements.

In addition to the study by Ottenio et al., two other works have been identified that analyze the mechanical properties of skin through uniaxial tensile tests, considering sample orientation and anatomical site of biopsy. In the study by Gallagher [25], tests were conducted on skin samples taken from cadavers to determine mechanical properties as a function of orientation and strain rate. Samples were tested at three different dynamic strain rates (1 m/s, 1.5 m/s, and 2 m/s) and prepared with three distinct orientations: parallel, 45°, and perpendicular to Langer's lines. Table 7 reports the mean values of the main mechanical properties (UTS, strain energy, elongation at break, and E) calculated by aggregating data from all samples (taken from the back) for each orientation, regardless of test speed.

Although this summary highlights the predominant effect of orientation, the detailed analysis also considers the influence of strain rate, in agreement with previous results, which showed that UTS and E of the skin increase with increasing strain rate. Consistent with these studies, the collected data also show that skin mechanical properties significantly depend on both orientation and strain rate, emphasizing the need to consider both factors in the analysis of skin biomechanical characteristics.

Table 7: Mean values of the mechanical properties of skin obtained from uniaxial tensile tests on cadaveric samples, divided by orientation relative to Langer's lines [25]. The data represents the average of measurements collected at three different dynamic strain rates (1 m/s, 1.5 m/s, and 2 m/s). Standard deviation (SD) is indicated in parentheses.

Reference	# Sample	Orientation	Strain rates	UTS [MPa]	Stretch ratio at failure	Strain Energy [MJ/ m^3]	E_2 [MPa]
Gallagher – 2012 [25]	9	Parallel	1, 1.5 and 2 m/s	30.5 (6.53)	1.22 (0.02)	5.24 (1.33)	127.22 (36.38)
	15	45°	1, 1.5 and 2 m/s	23.51 (6.53)	1.28 (0.06)	4.18 (1.44)	73.03 (15.84)
	9	Perpendicular	1, 1.5 and 2 m/s	29.82 (12.77)	1.26 (0.04)	5.7 (1.5)	117.14 (58.81)

Another analysis is presented in the study by Annaidh et al. [26], which jointly considers the orientation relative to Langer's lines and the anatomical location on the back (Upper, Central, Lower). Table 8 reports the mean values and standard deviations of the main mechanical properties (UTS, strain energy, elongation at break, and E) for each combination of orientation and location. This arrangement allows for a more precise understanding of the spatial variability of skin properties and provides quantitative support for the study's statistical conclusions, which state that both orientation and location significantly influence the mechanical response of the tissue.

Table 8: Mean values and standard deviations of the mechanical properties of excised human skin, categorized by orientation relative to Langer's lines and anatomical location on the back [26]. Standard Deviation (SD) is indicated in parentheses.

Reference	# Sample	Orientation	Location	Strain rates [s^{-1}]	UTS [MPa]	Stretch ratio at failure	Strain Energy [MJ/m^3]	E_2 [MPa]
Annaidh – 2012 [26]	9	Parallel	Middle	0.012	28.64 (9.03)	1.46 (0.07)	4.28 (1.49)	112.47 (36.49)
	7		Bottom		17.60 (4.77)	1.74 (0.32)	2.54 (0.76)	73.81 (19.41)
	12	45°	Top		22.7 (3.61)	1.52 (0.10)	3.80 (0.92)	82.62 (17.36)
	9		Middle		28.85 (7.87)	1.52 (0.15)	5.38 (2.59)	103.49 (41.20)
	5		Bottom		20.23 (4.18)	1.43 (0.04)	3.31 (0.67)	82.81 (18.43)
	9	Perpendicular	Middle		16.53 (5.71)	1.52 (0.08)	2.98 (0.89)	63.75 (24.59)
	5		Bottom		10.56 (8.41)	1.61 (0.14)	2.44 (1.04)	37.66 (36.41)

In addition to tensile tests, several authors have proposed the use of in-vivo indentation tests for the mechanical characterization of skin tissues. Boyer et al., Zahouani et al., and Pailler-Mattei et al. [27] [28] [29] have conducted studies on the forearm area, employing indentation as a non-invasive method to estimate the mechanical properties of skin under physiological conditions. These studies also consider environmental factors such as temperature and humidity, which can influence the mechanical response of the tissue.

One of the most notable aspects of Boyer et al.'s study is the calculation of the Young's modulus as a complex modulus E*, derived from dynamic indentation data under sinusoidal loading. This complex modulus consists of a real part, representing the elastic behavior of

the tissue, and an imaginary part, describing the viscous behavior, thus allowing a more comprehensive characterization of the skin's viscoelastic nature.

Table 9: Results' overview of *in-vivo* studies based on skin indentation tests. For each study, the following information are reported: number of samples analyzed, skin layers considered, age range of subjects, anatomical site examined, environmental conditions during testing in terms of temperature and relative humidity (RH), and values of the complex modulus E*. Standard deviation, where available, is reported in parentheses.

Reference	# samples	Layers	Age	Anatomical Site	Conditions	E* [kPa]
Boyer - 2009 [27]	16	Total skin	18-30	Right forearms	22 ± 1°C e 50% RH	10.7 (2.64)
	15		31-50			8.09 (1.84)
	15		51-70			7.17 (2.06)
Zahouani – 2008 [28]	20	Total skin	55-70	Forearms	22 °C e 50% RH	8.3 (2.1)
Pailler-Mattei - 2007 [29]	10	Dermis	≈30	Forearms	22 °C < T < 24 °C 20% < RH < 30%	35
		Hypodermis				2
		Muscle				80

A relevant contribution to the biomechanical characterization of human skin comes from experimental study by Barreiro et al. [30], which evaluated the tensile strength of abdominal skin in samples obtained from 25 patients (15 undergoing aesthetic abdominoplasty and 10 post-bariatric panniculectomy). Skin samples, measuring 32x20mm, were tested both in the craniocaudal (vertical) and transversal (horizontal) directions and the results were compared with four different types of meshes commonly used for hernia repair (high – and low – density polypropylene, polytetrafluoroethylene – PTFE, and porcine small intestinal submucosa).

The results showed that:

- The maximum tensile strength supported vertically by the abdominal skin was 403.5 ± 27.4 N in the aesthetic group and 425.9 ± 33.9 N in the post-bariatric group.
- In the horizontal direction, the values increased to 596.5 ± 32.2 N and 612. ± 43.9 N, respectively.

- No statistically significant differences were found between the 2 patient groups, while the difference between traction directions was highly significant.
- The tested meshes exhibited much lower strength values: high-density polypropylene 104.6 N, low-density polypropylene 54.4 N, PTFE 82.2 N, and porcine small intestinal submucosa 60.6 N.

These data demonstrated that human abdominal skin exhibits a tensile strength markedly superior to that of the main commercial prostheses. Furthermore, the higher resistance observed in the horizontal direction provides practical indications for the orientation of the skin flaps or potential derma grafts during abdominal wall reconstructive surgery.

The study of Barreiro et al. [30] reported the results of the mechanical tests of abdominal skin in terms of maximum force [N]. To allow comparison with the data already presented in the previous tables, the values were converted into $Ultimate\ Tensile\ Strength\ (UTS)$ using the following relation:

$$UTS\ [MPa] = \frac{Peak\ Force\ [N]}{A\ [mm^2]} \quad (1)$$

It must be noted, however, that $Peak\ Force$ represents the maximum force measured in N by Barreiro et al. [30], whereas A, the cross-section area subjected to tension, required information on sample thickness (Eq. 2), which is not provided in the cited article.

For this reason, we assumed an average thickness value calculated from previously presented mean epidermal and dermal thicknesses (Table 5) and used to estimate the cross-sectional area. Additionally, the maximum force values reported by Barreiro for the two patient groups were averaged for each direction, maintaining the distinction between longitudinal and transverse measurements. The resulting mean forces were then used to calculate the corresponding UTS values.

By considering an average thickness of 1.674 mm, the corresponding cross-sectional area (A) was calculated as:

$$A = width\ (mm) * thickness\ (mm) \quad (2)$$

and used to convert the original force values into stress. Using this approach, we obtained a longitudinal UTS of 12.4 MPa and a transverse UTS of 18.0 MPa.

As emerges from the comparative analysis of literature, the mechanical strength values of human skin show considerable variability. This difference is related to several factors: the

intrinsic anisotropy of the tissue (e.g. according to Langer's lines orientation for the back), individual variability, the anatomical site of sampling, as well as the experimental methodologies adopted.

Table 10: Mean UTS [MPa] values and SD (Standard Deviation) of abdominal skin samples, categorized by fiber orientation (longitudinal and transverse). SD is reported in parentheses.

Reference	Anatomical Part	# samples	Orientation	UTS [Mpa]
Barreiro – 2019 [30]	Abdomen	50	Vertical	12.40 (0.91)
		50	Horizontal	18.00 (1.14)

Such heterogeneity is evident not only in the study by Barreiro et al., but also in the previously reported works (Table 6, Table 7, Table 8, Table 9). For this reason, to establish a coherent reference model, this study primarily considers the average values of the general mechanical properties of the skin, regardless of the anatomical region or specific testing methodology, thereby obtaining a synthetic and consistent dataset suitable for simulation purposes.

Table 10: Summary of the mean mechanical properties of human skin obtained from literature, calculated as the average of the main studies analyzed. Values represent global averages independent of anatomical site or experimental methodology, used as reference data simulation purposes. SD is reported in parentheses.

Reference	Properties	# samples	Mean Value
Ottenio – 2014 [24] Gallagher – 2012 [25] Annaidh – 2012 [26] Barreiro – 2019 [30]	UTS [Mpa]	288	19.51 (3.62)
Ottenio – 2014 [24] Gallagher – 2012 [25] Annaidh – 2012 [26]	E_2 [Mpa]	188	101.34 (30.10)
Ottenio – 2014 [24] Gallagher – 2012 [25] Annaidh – 2012 [26]	Stretch ratio at failure	188	1.36 (0.10)
Ottenio – 2014 [24] Gallagher – 2012 [25] Annaidh – 2012 [26]	Strain Energy [MJ/ m^3]	188	4.83 (1.78)

4 Materials and Methods

4.1 3D-Printing Technologies

The present work is focused on the development of 3D-printed skin models leveraging Stratasys Digital Anatomy® solutions, namely J750, J850 and J5 (Figure 9). Digital Anatomy® printers are based on an additive manufacturing technology called *Material Jetting*, based on the selective deposition of microscopic droplets of liquid photopolymer onto a build platform using inkjet printheads, following a layer-by-layer approach [31]. During fabrication, one or multiple photopolymeric materials are precisely jetted and immediately cured by ultraviolet (UV) light, resulting in parts with excellent dimensional accuracy and very smooth surface finish. A dedicated support material is deposited simultaneously to stabilize overhangs and complex geometries and is subsequently removed by chemical or mechanical post-processing. Owing to the small droplet size and accurate droplet placement, Material Jetting enables high-resolution features as well as true multi-material and multi-color integration within a single component.

More specifically, Digital Anatomy® printers are based on the proprietary PolyJet™ technology, which is a multi-material, full-color system specifically optimized for creating lifelike anatomical models with realistic biomechanical behavior. The J750 and J850 share a large build volume (about 490 × 390 × 200 mm) and can jet an extremely wide palette of materials in more than 500,000 color and property combinations, including rigid Vero® family resins, flexible Agilus30™, transparent VeroClear/VeroUltraClear, and dedicated Digital Anatomy® materials such as TissueMatrix® (MED310C), BoneMatrix® (RGD516), GelMatrix® (FLG110) and RadioMatrix™ (MED410) resins. This combination allows the J750 and J850 to reproduce bone, myocardium, vasculature and radiopaque structures with validated haptic and imaging realism for training, pre-operative planning and device testing. The J5 Digital Anatomy® offers the same Digital Anatomy® material ecosystem and anatomically accurate presets in a more compact, “facility-friendly” platform with six independent material channels, enabling multi-color, multi-material, patient-specific models that replicate the look, feel and responsiveness of human anatomy while fitting smaller labs and clinical environments (https://www.stratasys.com/).

Material deposition can be precisely controlled by the proprietary software GrabCAD Print and the module Digital Anatomy® Creator (DAC), an advanced software add-on enabling fine-grained control over digital anatomical model creation for the Digital Anatomy® 3D-

printing platform (Figure 10). The module allows slice-by-slice material control of each print, enabling the calibration of digital materials to meet exact specifications and to customize internal structures to achieve a specific anatomical outcome (https://www.stratasys.com/). Users may select from anatomical presets already available, or invoke DAC to define new presets, adjust mechanical behavior, assign materials to individual layers or voxels, and then print directly via the GrabCAD Print interface.



Figure 9: Stratasys J850 Digital Anatomy® (left) and J5 Digital Anatomy® (right) printers (https://www.stratasys.com/).

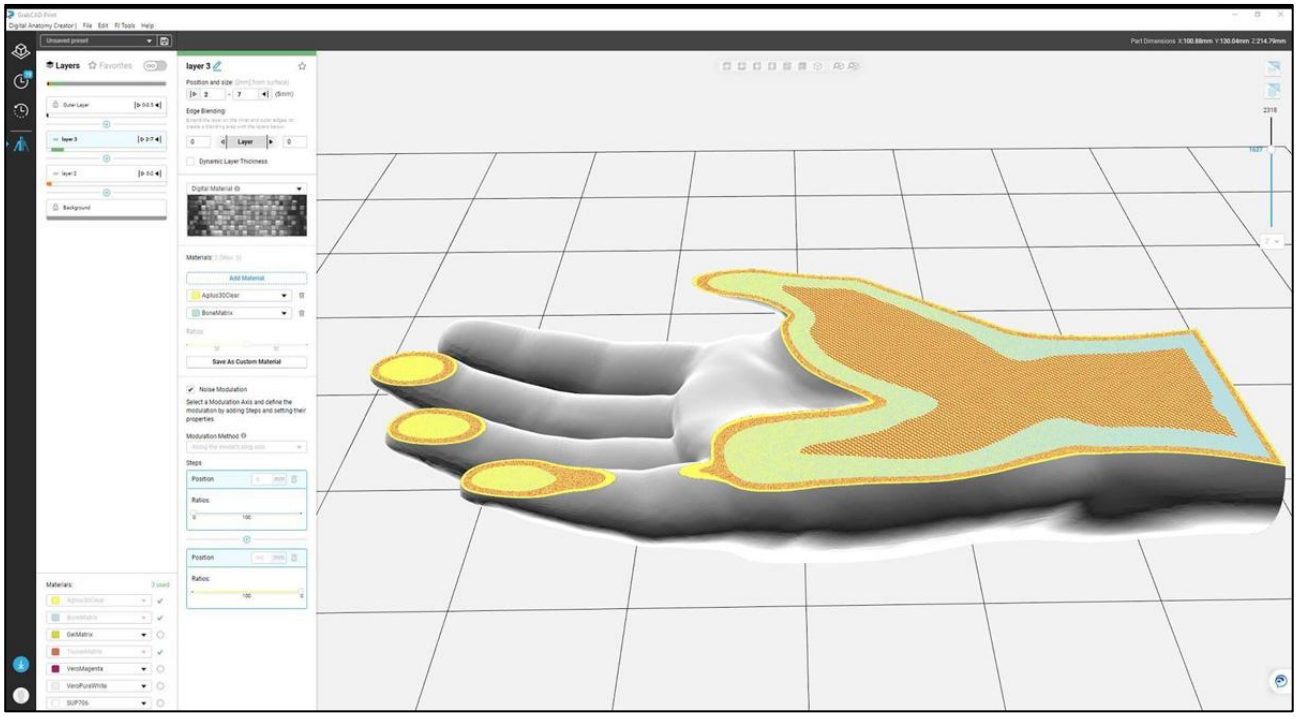


Figure 10: Digital Anatomy® Creator software interface overview (https://www.stratasys.com/).

4.2 Samples preparation

4.2.1 Ex vivo Abdominal Skin Samples

The literature review clearly shows a heterogeneity of results depending on the anatomical area, but also a limited amount of experimental data. Furthermore, there are no specific characterizations in the literature that can provide information on tissue performance during typical actions involving the skin during surgery, i.e. puncture, cutting and suturing. For this reason, we have set up an experimental characterization campaign on ex vivo human tissue samples, provided by the company GenoSkin (https://genoskin.com/).

Full-thickness human skin samples without adipose tissue were obtained from two female donors undergoing abdominal surgical procedures. The tissues were collected and processed in compliance with French regulations governing the use of human biological materials for scientific research (French law L.1245 CSP). Each sample was recovered fresh and subsequently processed within 24 hours to produce FrozenSkin® tissue substrates for in-vitro applications. Donor serum was screened for major viral pathogens (HIV-1/2, HBV, HCV, and SARS-CoV-2), and all results were negative.

Following macroscopic inspection, both skin samples were confirmed to be free of scars and stretch marks. The samples were maintained between +4°C and +15°C during recovery and transported on dry ice to the laboratory. Upon arrival, they were stored at –20°C until use. The collected specimens differed in donor age, Fitzpatrick skin phototype [32], and available surface area, as detailed in Table 11. In the following, the two samples will be referred to as “31Y, F” and “59Y, F” respectively.

The samples were left at room temperature for 1 hour to allow the tissue to thaw completely before proceeding with sample preparation. Four types of samples were obtained for uniaxial tensile testing, puncture testing, suture tensile testing and cutting testing, respectively, described in the following paragraphs. The samples for the individual tests were cut from the main sample using a surgical scalpel (blade #10). The mechanical tests were performed within a maximum of 3 hours after thawing.

Table 11: Ex vivo abdominal skin samples main features.

Parameter	31Y, F	59Y, F
Sex	Female	Female
Age (years)	31	59
Anatomical site	Abdomen	Abdomen
Fitzpatrick skin type	Not reported	Type 3
Surface area (cm²)	23.3	40.67
Product type	Full-thickness skin, without adipose tissue	Full-thickness skin, without adipose tissue
Surgery date	18 June 2025	16 July 2025
Production date	19 June 2025	17 July 2025
Testing date	23 June 2025	22 July 2025
Viral screening (HIV-1/2, HBV, HCV, SARS-CoV-2)	Negative	Negative
Macroscopic assessment	No scars or stretch marks	No scars or stretch marks
Delivery and storage	Transport on dry ice; storage at −20°C	Transport on dry ice; storage at −20°C

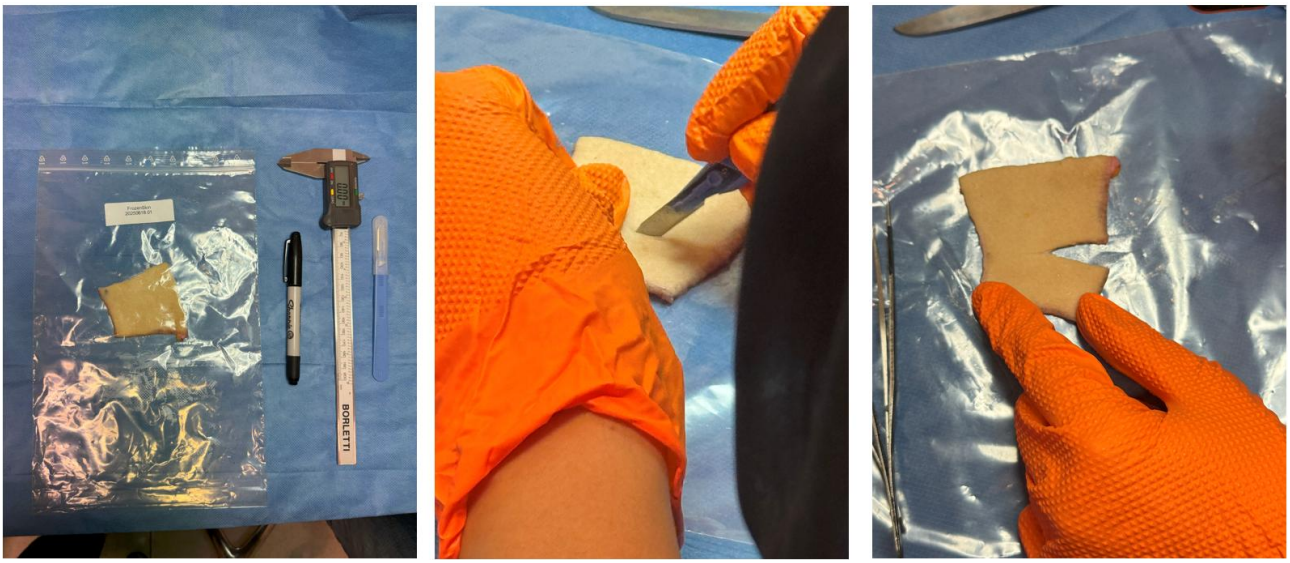


Figure 11: Ex vivo skin samples preparation after thawing.

4.2.2 3D-Printed Samples

The 3D-printed samples used for the mechanical tests were designed in Autodesk Inventor Professional 2025 and manufactured using either a J750™ or a J5™ Digital Anatomy™ printer. Print preparation was carried out in GrabCAD Print, using the DAC module to define the different material configurations. Samples printed on the J750 were produced at the Department of Civil Engineering and Architecture, University of Pavia, Pavia, Italy, where all mechanical testing was also performed. Samples printed on the J5 were produced at Stratasys facilities in Rehovot, Israel, and shipped directly as removed from the build tray, without cleaning or additional post-processing. All samples were printed with Matte finishing and Heavy Support options, as these are expected to be the recommended printing conditions for patient-specific, complex anatomical models. After printing, specimens were manually cleaned to remove most of the support material and then immersed for 2 hours in a cleaning solution containing 2% sodium hydroxide and 1% sodium metasilicate, Na_2SiO_3. They were then rinsed under tap water and immersed in a 15% solution of technical-grade glycerol, 99% purity, for 30 seconds. Samples were left to dry for at least 12 hours at room temperature before testing [33].

Dry cleaning was applied only to peeling test samples due to constraints imposed by their geometry. In these specimens, the inner layers are laterally exposed, and wet cleaning could alter the interfaces and compromise the measured peeling force.

4.3 Mechanical Testing Set-up and Testing Protocols

Uniaxial tensile tests on skin samples were performed using an MTS Insight testing machine equipped with a 10 kN load cell. Puncture, suture traction, cutting, and peeling tests were carried out using a TA ElectroForce biaxial planar testing machine equipped with a 45 N load cell. A custom mechanical setup was developed and optimized for both 3D-printed and ex vivo specimens. All tests were performed under displacement control at a constant deformation rate. Specific details for each test are reported below.

4.3.1 Uniaxial Traction Test

Although no ASTM standard is specifically dedicated to uniaxial tensile testing of human soft tissues, ASTM D638 (*Standard Test Method for Tensile Properties of Plastics)* provides a useful methodological framework for defining specimen geometry, clamping, and test speed when working with flexible polymeric materials. Given the structural and mechanical similarities between soft polymers and biological tissues in terms of viscoelastic behavior, this standard was used as the primary reference for setting up the test protocol.

According to ASTM D638, tensile tests may be performed at cross-head speeds ranging from 1 to 500 mm/min, depending on the material type and specimen dimensions. Within this recommended range, a displacement rate of 20 mm/min was selected for the present study, ensuring controlled deformation while avoiding dynamic effects that could compromise measurement accuracy.

Samples with an average area of 9.6 × 24.7 mm were extracted from the abdominal skin specimens, following the general principles of ASTM D638 with respect to consistent gauge length and specimen preparation. High-clamping-force mechanical grips and alignment procedures were adopted to minimize slippage and ensure uniform stress distribution during testing. A total of ten samples were prepared from the two ex vivo skin specimens. Four valid tests were obtained from the 31Y, F specimen along the vertical direction, while additional samples were used to tune the test setup. Six specimens were obtained from the 59Y, F specimen, three oriented along the horizontal direction of the abdomen and three along the vertical direction, to assess the intrinsic anisotropy of the tissue.

Results are presented in terms of $Peak\ Force$, that is the maximum force value detected by the load cell during the test, UTS (Eq. 1) and $Elastic\ Modulus\ (E)$, which describe the

relation between longitudinal stress applied (σ) and the strain developed in material (ε) up to the proportionality limit for the elastic behavior ($E = \frac{\sigma}{\varepsilon}$).

.

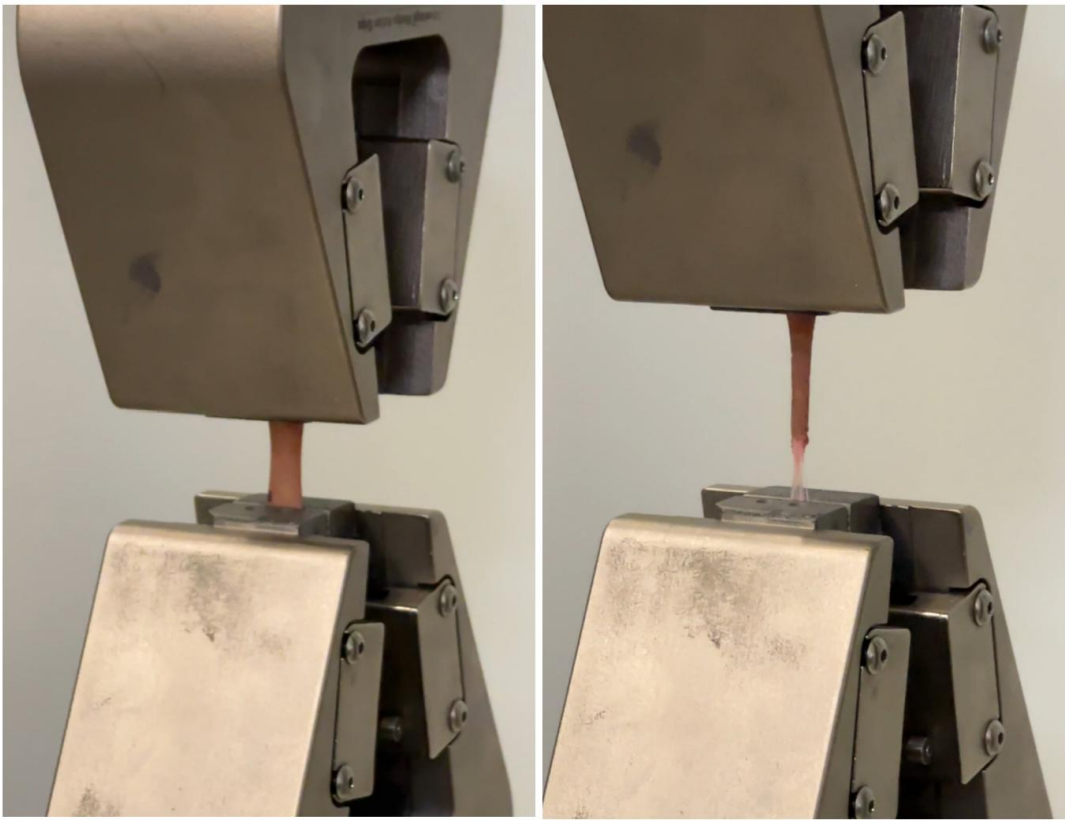


Figure 12: Uniaxial traction test on an abdominal sample at the beginning (left) and the ending (right) of the test.

4.3.2 Puncture Test

Puncture tests were conducted with reference to ASTM D2582-03 and ASTM F1342-91 (R96). ASTM D2582-03 specifies a method for evaluating the dynamic tear resistance of plastic films and thin sheets under snag-type conditions, whereas ASTM F1342-91 (R96) describes a procedure for assessing puncture resistance by measuring the force required for a sharp probe to penetrate a material.

The 3D-printed samples featured a circular geometry with a diameter of 26 mm and included the skin layer only, whereas the ex vivo samples were cut into square specimens with a side length of approximately 15 mm.

The custom setup developed for this study consists of two primary components:

1. Sample Holder:

   The holder comprises a drawer system and two clamping plates for securing the specimen. The plates can be customized to accommodate different specimen thicknesses. For ex vivo skin samples, the plates were modified to improve fixation throughout the test. The tissue samples were glued around the perimeter of the central opening. The hole diameter was reduced from 20 mm (used for 3D-printed samples) to 13 mm to prevent excessive deformation during puncture.

2. Needle Holder:

   The needle holder is mounted on the actuator which is equipped with a load cell to record puncture forces. A Trusilk™ 4-0 Straight Round-Bodied 19 mm needle was used for all tests. To avoid artefacts associated with tip wear, a new needle was used at the beginning of each testing session.

During testing, the needle advanced at a speed of 5 mm/s while the sample holder remained stationary. Force and displacement were continuously recorded at a sampling rate of 200 Hz.

Results are presented in terms of puncture $Peak\ Force$, that is the maximum force value detected by the load cell during the test, and puncture $Unit\ Peak\ Force$ that is computed as follow:

$$Unit\ Peak\ Force\ \left[\frac{N}{mm}\right] = \frac{Peak\ Force\ [N]}{T_s\ [mm]} \tag{3}$$

where T_s is the sample's thickness.

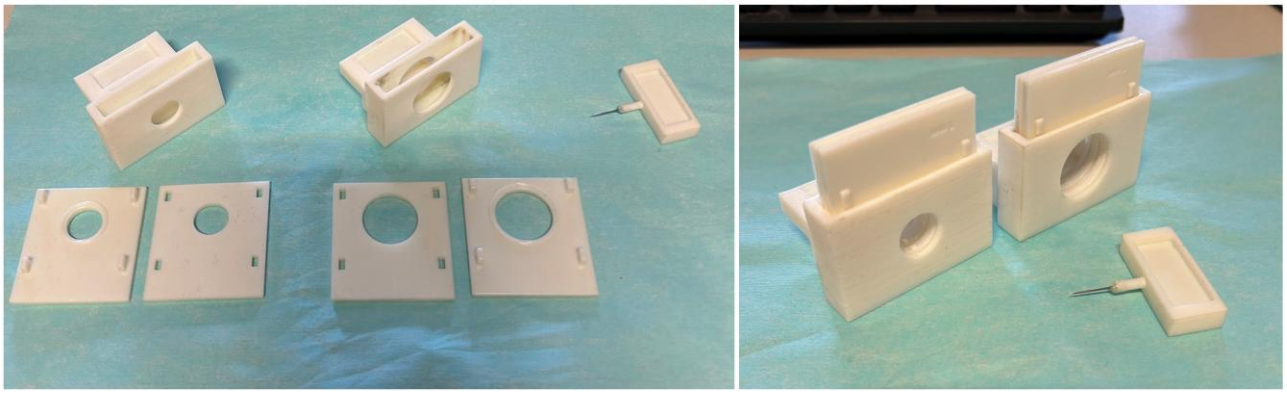


Figure 13: Puncture test custom device for ex vivo skin samples (13 mm diameter hole) and 3D-printed samples (20 mm diameter hole) respectively.

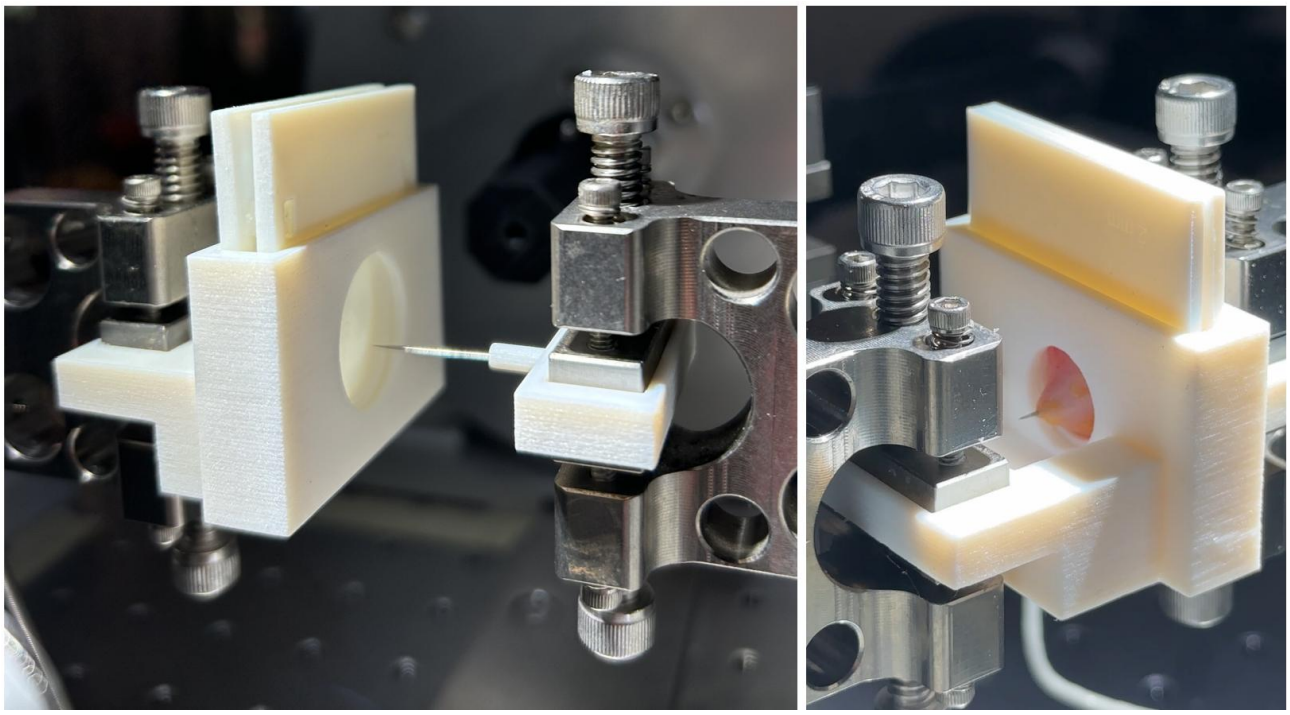


Figure 14: puncture device system mounted on the biaxial testing machine, for 3D-printed materials (left) and ex vivo skin sample (right) respectively.

4.3.3 Suture Traction Test

To perform the suture traction test, rectangular specimens measuring 10 × 45 mm were 3D-printed and then cut in half, yielding two samples of approximately 10 × 22.5 mm. Samples included the skin layer only. The same dimensions were used to prepare the ex vivo skin specimens. A single stitch was placed through the middle of the cut edge using a suture filament, 3-0 ETHILON* Polyamide 6, 3/8 circle, 19 mm (Figure 15).

Each specimen was clamped at one end, leaving a predefined free length of 9 mm available for loading. The opposite end was connected to a hook via the single suture stitch. During testing, the two ends were displaced in opposite directions at a rate of 5 mm/s.

Results are presented in terms of the following derived parameters:

$$Ultimate\ Stress\ \left[\frac{N}{mm^2}\right] = \frac{Peak\ Force\ [N]}{n * T_f\ [mm] * T_s\ [mm]} \quad (4)$$

where $Peak\ Force$ is the maximum force value detected by the load cell during the test, n is the number of stitches here equal to 1, T_s is the sample's thickness and T_f is the suture's filament thickness equal to 0,23 mm.

$$Normalized\ Max\ Displacement\ \left[\frac{1}{mm}\right] = \frac{Displacement\ [mm]}{D_b\ [mm] * T_S\ [mm]} \quad (5)$$

where $Displacement$ is the maximum displacement achieved by the grippers during the test, D_b is the measured distance between the free end of the sample and the suture-filament hole, which varies slightly among samples due to operator-dependent handling. This distance has a nominal value of 2,65 mm, retrieved from a preliminary analysis of sutures made by surgeons on real skin and 3D-printed samples.

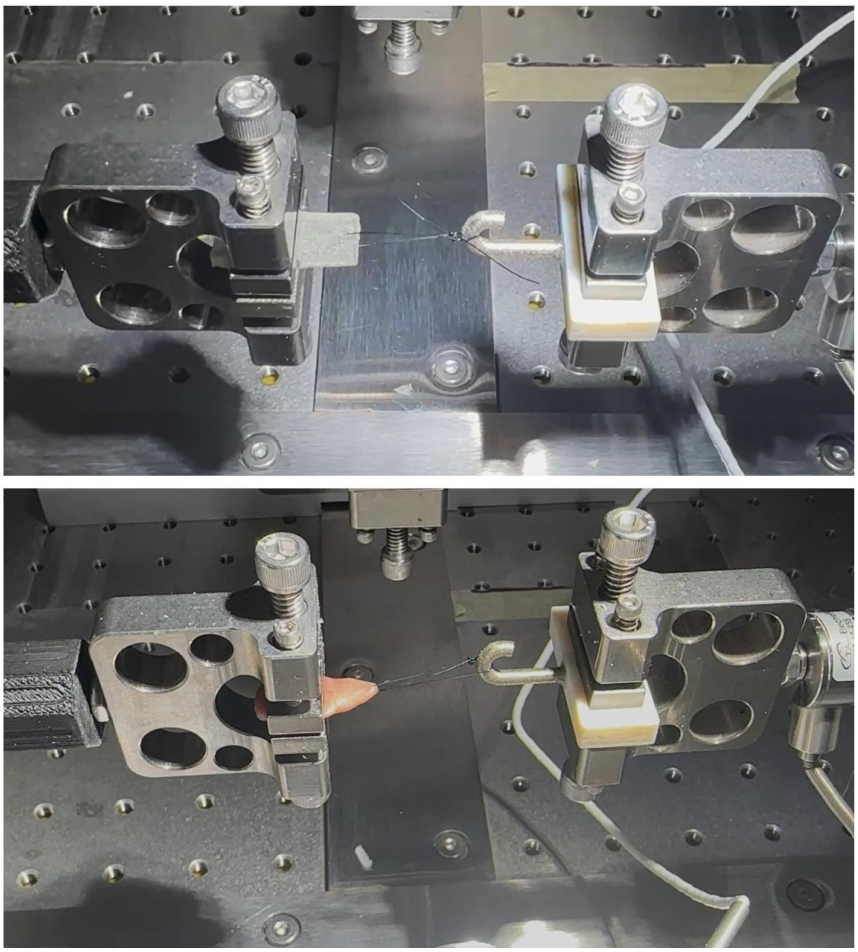


Figure 15: biaxial testing machine equipped for suture traction test on 3D-printed materials (up) and ex vivo skin sample (down) respectively.

4.3.4 Cutting Test

For the cutting test, ISO 13997:1999 was used as the reference standard. This standard specifies a method for determining the resistance of protective clothing materials to cutting by sharp edges.

The cutting test specimen was designed to include all layers contributing to surgical cutting feedback, namely the *skin*, in the different configurations under investigation, 3 mm of *subcutaneous fat* and 6 mm of *muscle* (Figure 16). A 1 mm thick lateral containment frame made of Agilus was added to prevent exposure of the subcutaneous fat layer, which can be easily damaged during cleaning. The subcutaneous fat and muscle layers were printed using the following pre-defined presets:

- Subcutaneous Fat: “General Anatomy → Subcutaneous Fat → Non-Encapsulated Highly Contractile”
- Muscle: “General Anatomy → Solid Internal Organs → Fibre Contraction 1”

A custom support was designed for the test, consisting of two components (Figure 17):

1. Sample holder

   This component included a base and an open clamping element secured together with screws. Its purpose was to hold the specimen in position while providing an open window that allowed the blade to pass through during the test.

2. Blade holder

   A dedicated support was fabricated to ensure consistent positioning of the scalpel blade on the biaxial testing machine.

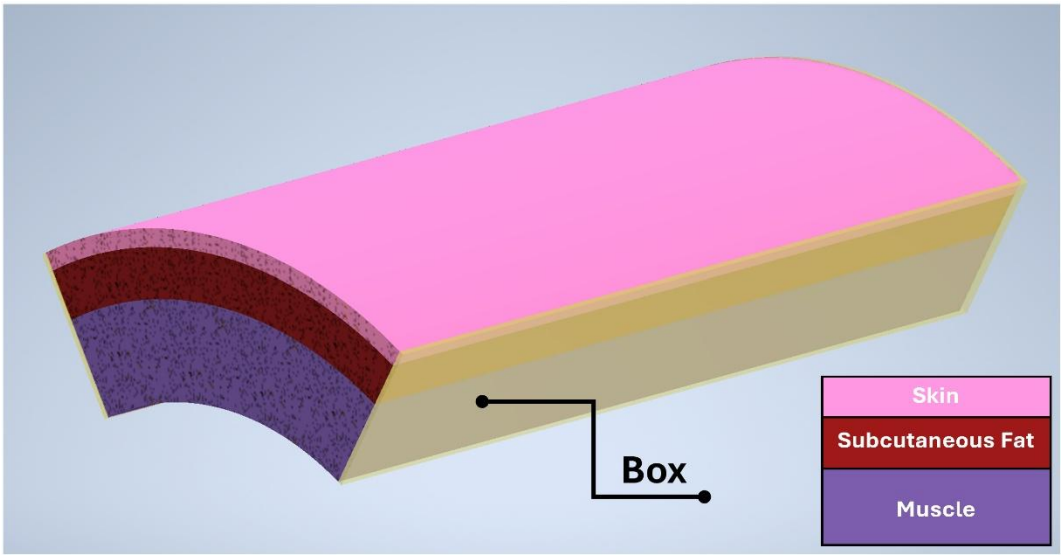


Figure 16: Cutting specimen design (cross-section view). It is composed of 3 layers, the skin, the subcutaneous fat (Non-Encapsulated Highly Contractile) and the muscle (Fibre Contraction 1) and it is laterally enclosed in an Agilus box.

As with the puncture test, the setup was adapted for the skin samples. The openings in both the base and the upper clamp were reduced in size to accommodate the smaller dimensions of the ex vivo skin specimens. Moreover, since these samples consisted solely of the epidermis and dermis layers, the setup included a 3D-printed layer of subcutaneous fat inserted below the skin sample to properly simulate the blade–tissue interaction (Figure 18).

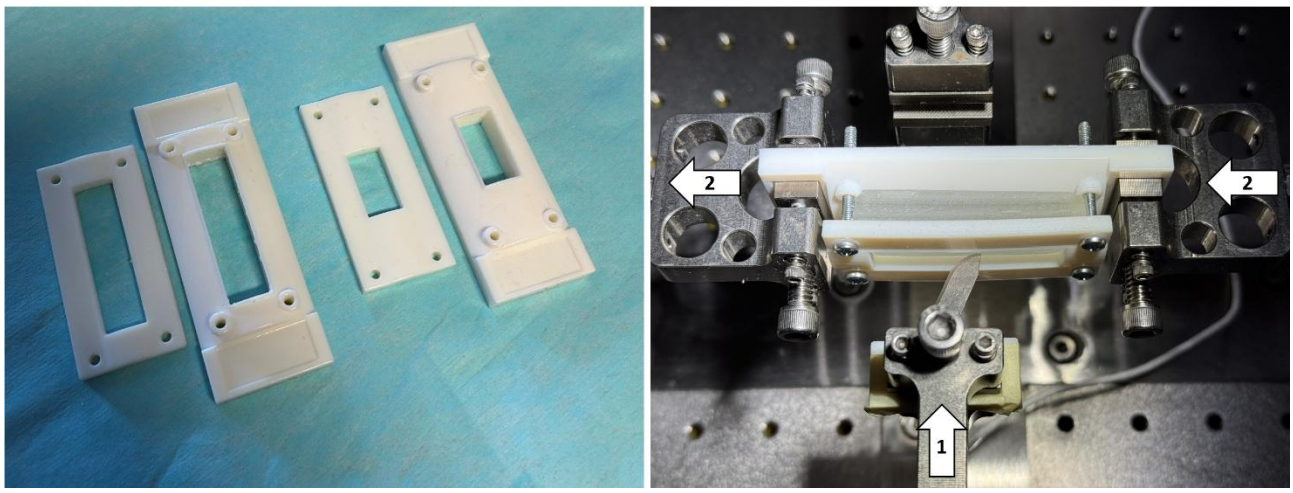


Figure 17: On the left, the sample holding device for 3D-printed samples (bigger window) and ex vivo skin samples (smaller window) respectively. On the right, the device mounted on the biaxial testing machine. The blade first moves towards the sample (1) and then in the orthogonal direction to perform the cut (2).

The cutting test was performed in two sequential phases. First, the blade penetrated the sample to a depth of 5 mm (direction “1” in Figure 17). To verify correct blade insertion, as

prescribed by the reference standard, the load values were monitored during penetration, ensuring they reached at least 6 to 10 N. Lower values may indicate incomplete insertion, whereas higher values may suggest interference preventing proper penetration. As a second step, the blade was drawn through the specimen at a speed of 2.5 mm/s for a total displacement of 12 mm (direction “2” in Figure 17).

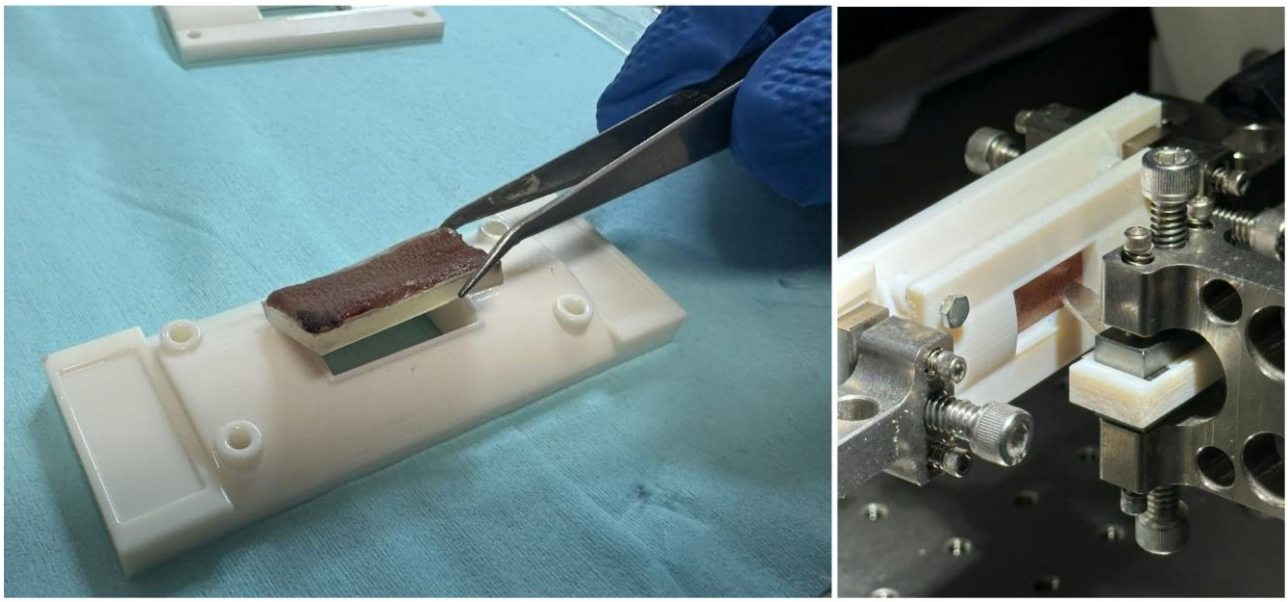


Figure 18: On the left, a detail of the ex vivo skin sample, which is place upon a 3D-printed subcutaneous fat layer. On the right, the device mounted on the biaxial testing machine.

4.3.5 Peeling Test

For the peeling test, ASTM D6862-11 (2021) was used as the reference standard. This standard describes a method for measuring the 90° peel resistance of an adhesive bond between a rigid substrate and a flexible adherend. The test was performed on 3D-printed samples only, as it was not possible to obtain a suitable sample from ex vivo specimens. In the present study, the reference standard was adapted to assess adhesion between two material layers, namely the *skin*, in the different configurations under investigation, and the *subcutaneous fat*, and to quantify the force required to separate them.

The specimen was designed with three rigid ends, printed in VeroPureWhite, to be secured in the grips, and a compliant region, printed in Agilus, located immediately above the interface to be tested (Figure 19). This compliant region enables the specimen to bend to 90° during testing. The gripped portions had a width of 20 mm and a thickness of 2 mm.

Their length was defined by the machine configuration, 72 mm for the upper arm and 80 mm for the lower arm. The layers of interest were positioned at the center of the specimen and overlapped over 12 mm, corresponding to the maximum displacement available on the biaxial testing machine. This overlap is the only region in which the upper and lower arms are in direct contact. The tested layers reproduced the thickness of the skin configurations under investigation, namely 0.8 mm and 1.1 mm. Additional Agilus and VeroPureWhite features were included to prevent tearing of the tested materials during traction.

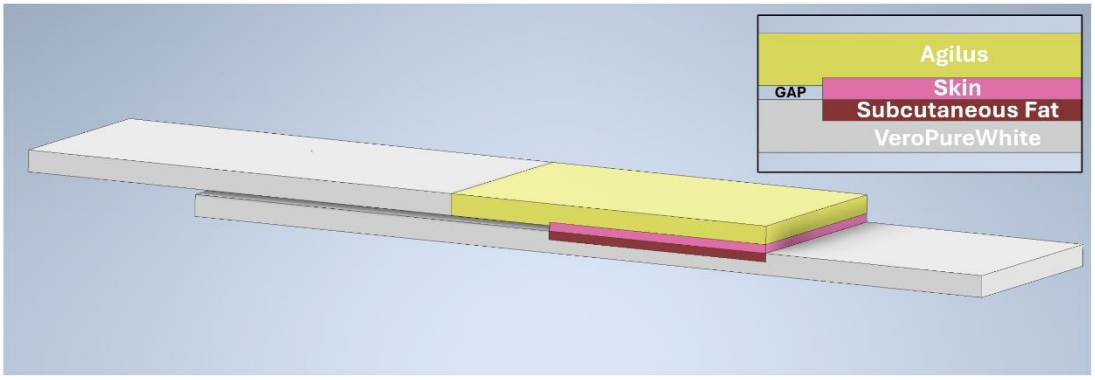


Figure 19: Peeling specimen design. The specimen includes three rigid ends secured in the grips and a central region in which only the two layers of interest are in contact. An additional Agilus layer enables 90° bending during peeling.

During testing, the specimen was secured using two grips moving in the same direction, allowing the sample to slide, while a third grip moving perpendicularly enabled peeling of the upper layer (Figure 20). All grips were driven at 2.5 mm/s, maintaining a constant 90° peel angle at the interface throughout the test. The force required to separate the two layers of interest was recorded.

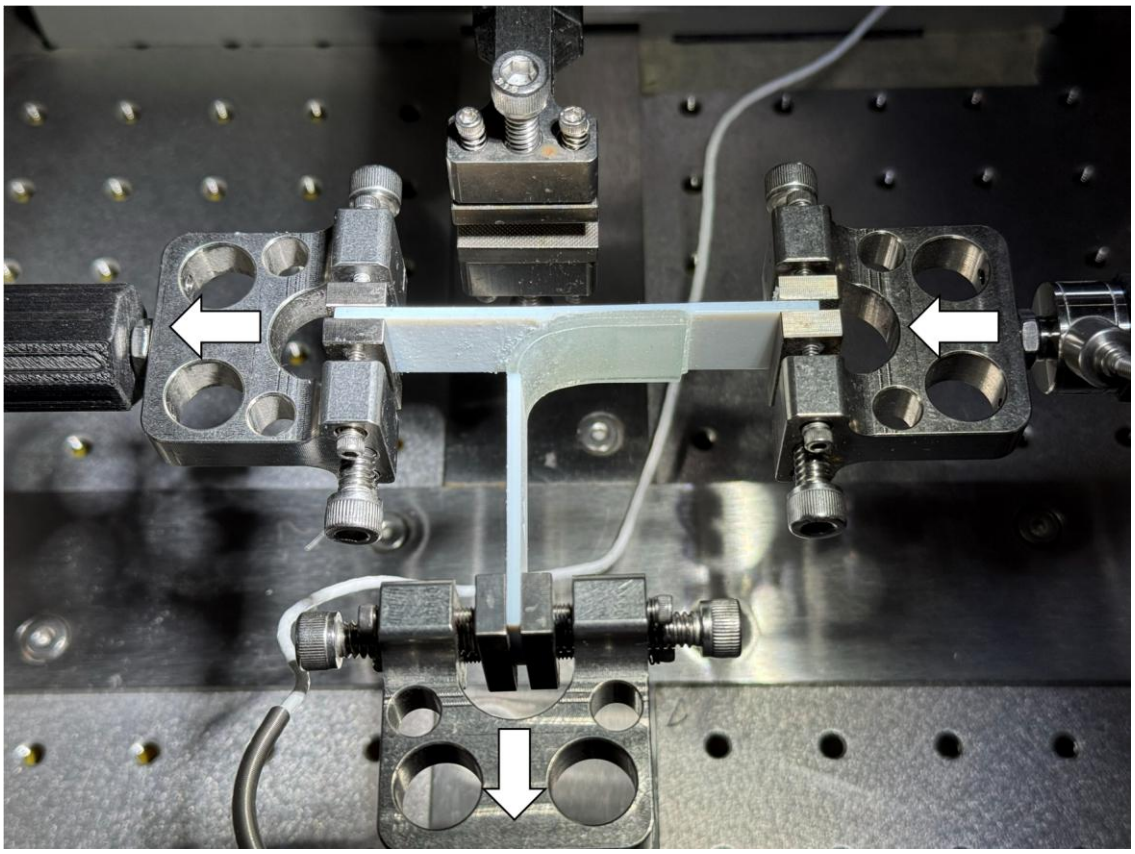


Figure 20: Peeling specimen used to assess adhesion between the muscle tissue and the temporal bone, mounted on the biaxial testing machine. Two grips move simultaneously in the same direction, while a third grip moves perpendicularly to maintain a 90° peel angle at the interface.

4.4 Qualitative Testing

In addition to the mechanical tests, qualitative assessments were performed by producing samples representative of the target anatomies on which the surgical procedures selected as application cases, namely oto-neurosurgery and laparoscopic abdominal surgery, would be carried out. Qualitative test samples were designed in Autodesk Inventor Professional 2025 and manufactured using a J750™ Digital Anatomy™ printer. Each sample featured a 40 × 40 mm area with a surface curvature approximating the natural anatomy of the corresponding region, more pronounced for the temporal bone and less pronounced for the abdomen. A completely flat surface was avoided, as it could bias the outcome due to the perfectly planar stratification of the printed layers. The samples were configured as shown in Figure 21. The white dotted line indicates the interface between the layers tested in the peeling test.

For the temporal region case, the sample consisted of:

- skin;
- subcutaneous fat;
- muscle;
- temporal bone.

The sample was laterally enclosed by a VeroPureWhite containment box.

For the laparoscopic abdominal surgery case, the sample consisted of the following layers:

- skin;
- subcutaneous fat;
- muscle layer;
- visceral fat layer.

Also in this case, the assembly was laterally enclosed by a containment box made of Agilus.

Skin layer is printed using the various DAC presets under development, while other layers are printed using already available presets according to previous knowledge as follows:

- Subcutaneous and visceral fat: General Anatomy → Subcutaneous Fat → Non-Encapsulated Highly Contractile
- Muscle: General Anatomy → Solid Internal Organs → Fibre Contraction 1
- Bone: VeroPureWhite

For the qualitative testing, the evaluation focused on the behavior of the skin layer during cutting and suturing.

For the laparoscopic abdominal surgery application, the qualitative test sample was subjected to an incision performed with a surgical scalpel (blade #10), down to the subcutaneous fat, followed by suturing.

For the oto-neurosurgery application, the following steps were simulated (Figure 22 and Figure 23): incision of the epidermis and dermis (blade #10), down to the subcutaneous fat, incision of the temporalis muscle, down to the temporal bone, using a multilayer incision as in real surgery, detachment of the temporalis muscle from the temporal bone and lastly skin suturing. The suturing of the temporalis muscle is omitted.

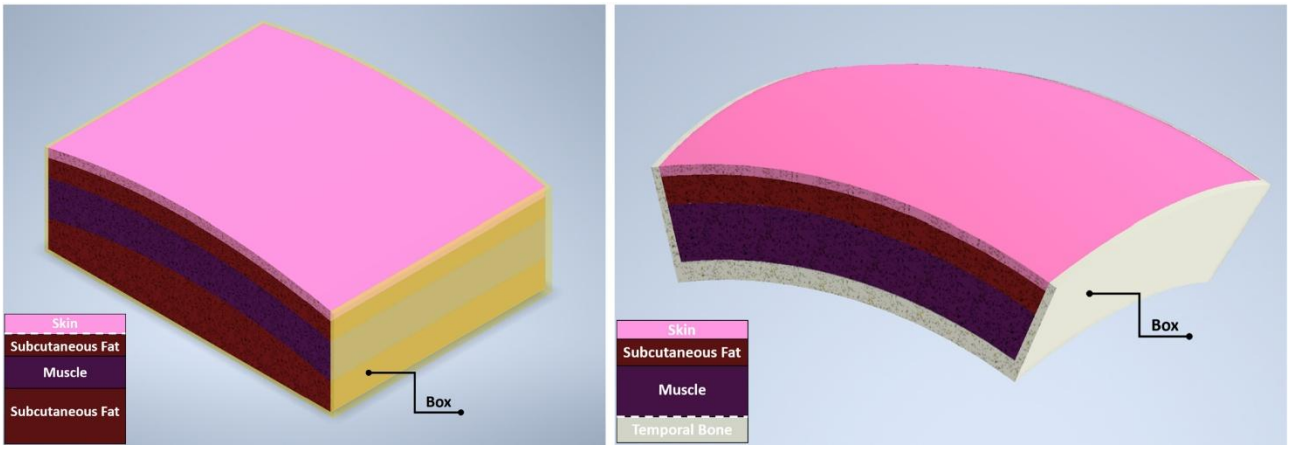


Figure 21: A cross-sectional view of the qualitative testing samples for abdominal surgery (left) and oto-neurosurgery (right) applicative cases to highlight the internal layer structure. The white dotted line represents the interface between the layers tested during the peeling test.

The following parameters were evaluated and combined with the results of the mechanical tests:

- overall feel, including skin appearance and compressibility;
- cutting behavior;
- needle insertion;
- filament sliding;
- skin retraction, defined as how the skin behaves when pulled to open the wound;
- detachment from subcutaneous fat (for the abdominal surgery case only);
- muscle to bone adhesion (for the oto-neurosurgery case only);
- stitch resistance, assessed by applying a traction force to simulate stitch removal.



Figure 22: Three steps of the qualitative testing procedure on the temporal bone model, including skin and muscle cutting (1), bone exposure (2) and muscle detachment from the temporal bone (3).

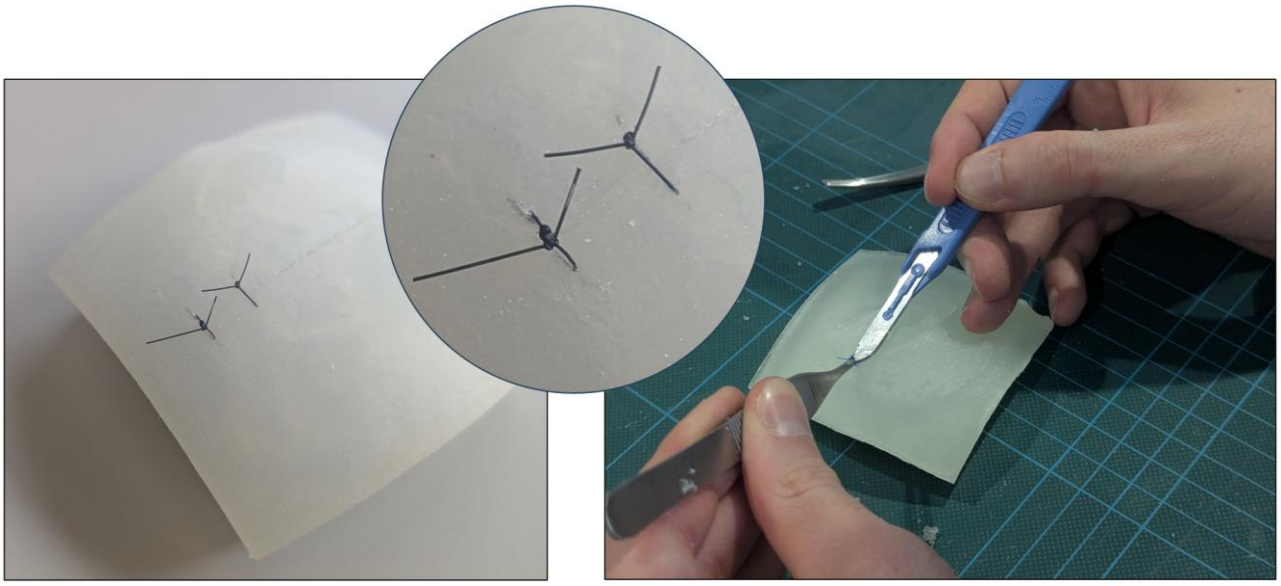


Figure 23: Temporal bone model at the end of the suturing (left) and during stitch resistance check (right).

5 Results

5.1 Abdominal Skin Mechanical Properties

According to the information provided by Genoskin, the orientation of the samples with respect to the body axis is as shown in Figure 24.

Sample 31Y, F is smaller in size and was mainly used to fine-tune the various mechanical tests. It was therefore possible to obtain a small number of valid samples.

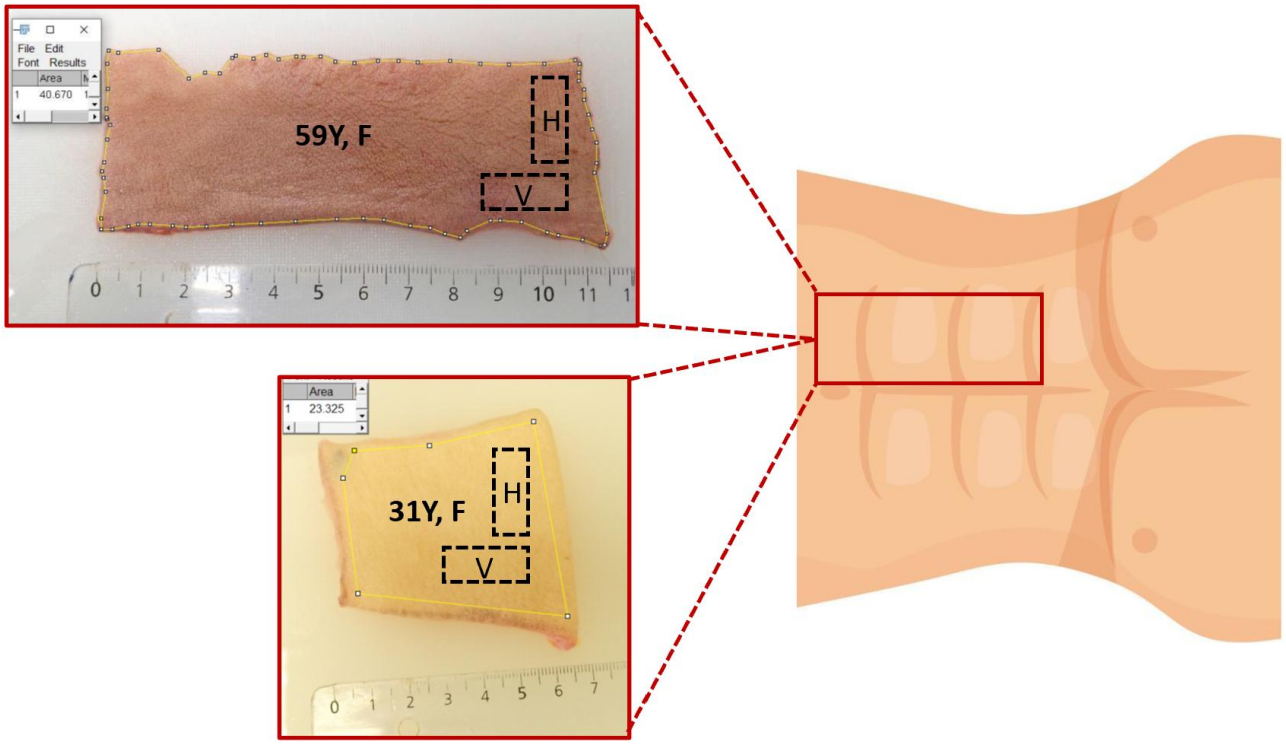


Figure 24: Scheme of the sample orientation with respect to the body axis.

5.1.1 Uniaxial Traction Test

Four valid samples were obtained from sample 31Y, F and six valid samples from sample 59Y, F. From sample 59Y, F, it was also possible to obtain samples in two orientations relative to the body axis, indicated respectively as vertical (V) and horizontal (H).

The results, reported in Table 12 and Table 13, are consistent with the limited data available in the literature. With increasing age, peak strength and average thickness decrease

significantly, whereas the effect on elongation at break is less pronounced. A clear difference is observed depending on orientation relative to the body axis, with higher peak strength values in the horizontal direction; again, the impact on elongation at break is smaller.

Literature data for patients undergoing abdominoplasty (i.e., the same procedure undergone by the patients from whom the samples were collected) report an average peak force of 500 N, with mean values of 403.50 N and 596.50 N in the vertical and horizontal directions, respectively. This corresponds to an increase of 47.8% from the vertical to the horizonal direction. The trend is consistent with our results, although we observed an increase of up to 225% in sample 59Y,F.

Even though it was not possible to obtain tensile specimens in the horizontal direction for sample 31Y, F, we can expect an increase in peak force ranging from a minimum of 47.8% (as reported in the literature) to 225% (as observed in internal tests on sample 59Y, F). The expected peak force in the horizontal direction is therefore between 458.46 N and 1007.50 N, which is consistent with the literature mean value of 596.50 N.

.

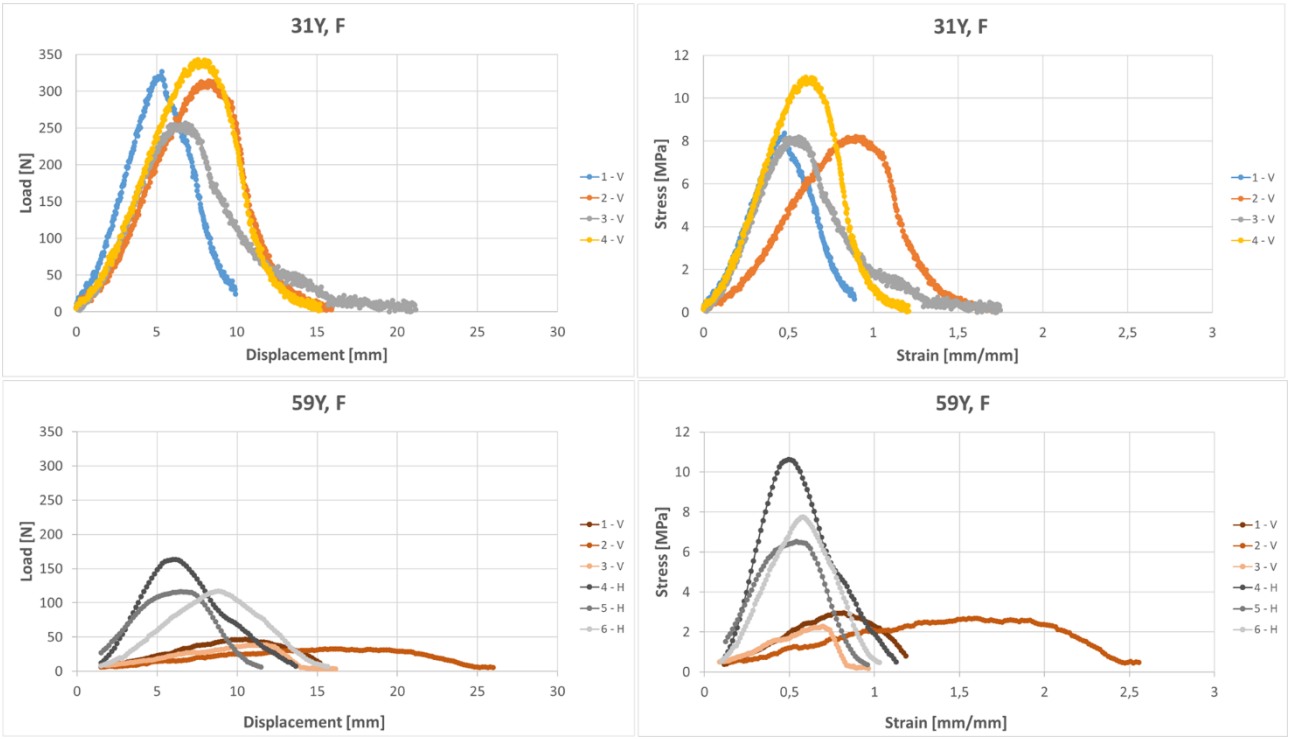


Figure 25: Results of the uniaxial traction test on the ex vivo skin samples.

Table 12: Samples data for uniaxial traction test.

	Sample ID	Test Data	Deformation Rate [mm/min]	Width [mm]	Length [mm]	Thikness [mm]	Cross Section [mm^2]	Grip Distance [mm]	Elastic Modulus [MPa]	Peak Force [N]	UTS [MPa]
31Y, F	1 - V	23/06/2025	20,00	11,32	26,78	3,45	39,09	11,16	21,02	326,96	8,36
	2 - V	23/06/2025	20,00	11,32	26,14	3,37	38,32	9,17	12,72	314,21	8,20
	3 - V	23/06/2025	20,00	10,72	25,31	2,93	31,45	12,10	19,72	256,57	8,16
	4 - V	23/06/2025	20,00	11,74	23,04	2,66	31,24	12,60	20,93	343,02	10,98
59Y, F	1 - V	22/07/2025	20,00	9,80	24,01	1,61	15,78	12,80	3,76	50,21	3,18
	2 - V	22/07/2025	20,00	8,53	22,42	1,43	12,20	10,17	1,86	36,80	3,02
	3 - V	22/07/2025	20,00	10,37	27,68	1,65	17,11	16,74	3,36	42,79	2,50
	4 - H	22/07/2025	20,00	9,38	22,60	1,64	15,38	12,12	27,14	177,89	11,56
	5 - H	22/07/2025	20,00	10,17	23,35	1,76	17,90	12,01	16,94	123,36	6,89
	6 - H	22/07/2025	20,00	9,21	28,00	1,64	15,10	15,22	15,55	120,34	7,97

Table 13: Average values for uniaxial traction tests for different ages and orientations with respect to the body axis.

			Thikness [mm]	Elastic Modulus [MPa]	Peak Force [N]	UTS [MPa]
31Y, F	V	Mean	3,10	0,55	**310,19**	8,93
		SD	0,37	0,08	37,64	1,37
59Y, F	V	Mean	1,56	2,99	**43,27**	2,90
		SD	0,12	1,00	6,72	0,36
	H	Mean	1,68	19,88	**140,53**	8,81
		SD	0,07	6,33	32,39	2,45
	V&H	Mean	1,62	11,44	**91,90**	5,85
		SD	0,11	10,10	57,23	3,59

5.1.2 Puncture Test

For the puncture test, one specimen was obtained from sample 31Y, F and four specimens from sample 59Y, F. The specimen from 31Y, F was used for five valid repetitions, performing the puncture at a different location each time. Each specimen from 59Y, F was tested in three repetitions: one in the center (Middle – M) and one in the upper (High – H) and lower (Low - L) portions of the specimen, respectively. For each test, puncture was performed while maintaining a safety margin from the specimen clamping/anchoring area to minimize edge effects.

Although the literature does not report puncture test results for comparison, the observed behavior is consistent with thinner and stiffer tissue with advancing age. Peak force values exhibit higher values for sample 31Y, F, which has an average thickness of 3.1 mm. In contrast, sample 59Y, F has an average thickness of 1.38 mm. Therefore, the Unit Peak

Force is higher for the 59Y, F sample due to its lower thickness, which is consistent with a progressive increase in stiffness of the superficial skin layers with age.

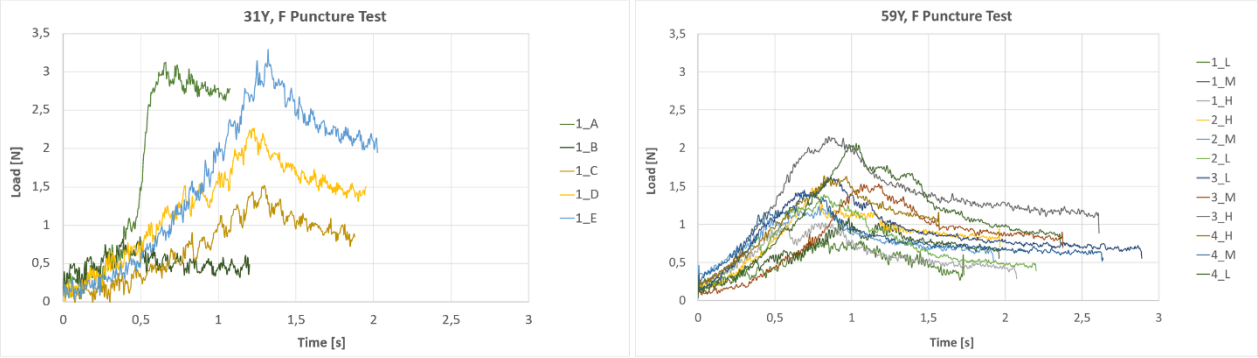


Figure 26: Results of the puncture test on ex vivo skin samples. For sample 59Y, F letters refer to the puncture location: High (H), Middle (M) and Low (L).

Table 14: Average values for puncture test for different ages.

31Y, F		Peak Force [N]	Unit Peak Force [N]
	MEAN	**2,21**	**0,71**
	SD	1,04	0,34
	RSD%	47,13%	47,13%
59Y, F		Peak Force [N]	Unit Peak Force [N/mm]
	MEAN	**1,45**	**1,07**
	SD	0,39	0,33
	RSD%	27,17%	31,12%

5.1.3 Suture Traction Test

There is no literature data available for comparison regarding suture tensile strength tests. Our results show higher peak values for younger tissue and lower values for older tissue, in line with evidence of reduced tissue thickness with advancing age and with surgeons' reports across different specialties describing lower suture holding strength in older patients.

It is important to note that the measured peak force corresponds to suture filament rupture, not skin rupture. This should not be considered a limitation of the study, since the force applied by the surgeon during suturing should never reach values high enough to cause filament failure. For this reason, we will refer to the average Ultimate Stress computed for

the 31Y, F sample as a safe limit to compare the result of 3D-printed samples, knowing that this is the hardest parameter to simulate.

The measured distance between the free end of the sample and the suture-filament hole on all the tested samples has a value of 2.73 ± 0.37 mm, in line with the nominal value of 2.65 mm. The average measured thickness is 3.1 mm for 31Y, F samples and 1.62 mm for 59Y, F samples respectively, leading to a higher Ultimate Stress for the latter.

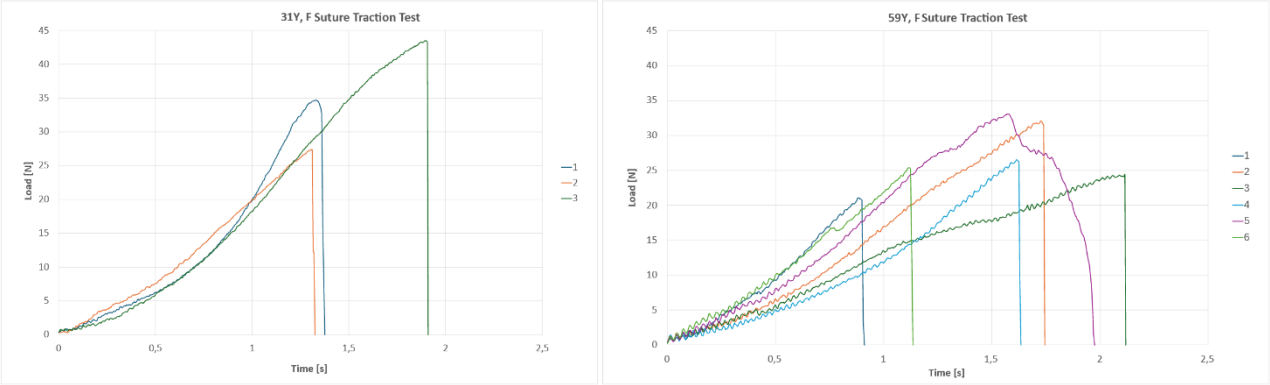


Figure 27: Results of the suture traction test on the ex vivo skin samples.

Table 15: Average values for suture traction tests for different ages.

		Peak Force [N]	Ultimate Stress [N/mm2]	Max Displacement [mm]	Max Displacement Norm [1/mm]
31Y, F	**MEAN**	**35,21**	**49,38**	**7,59**	**0,80**
	SD	8,10	11,36	1,63	0,27
	RSD%	23,01%	23,01%	21,49%	33,32%
59Y, F		Peak Force [N]	Ultimate Stress [N/mm2]	Max Displacement [mm]	Max Displacement Norm [1/mm]
	MEAN	**27,08**	**73,13**	**7,91**	**1,95**
	SD	4,64	14,04	2,36	0,60
	RSD%	17,12%	19,20%	29,88%	30,73%

5.1.4 Cutting Test

As for the suture and puncture tests, no literature data are available for comparison for the cutting test either. The specimen required for the cutting test is substantially larger than those used in the previous tests, therefore only one test was performed. The test provided information on the sliding force required to cut through the tissue, using a surgical scalpel (blade #10) inserted 5 mm into the skin. The force reached a maximum of 3.98 N and then plateaued at approximately 3 N.

The peeling test could not be performed on ex vivo skin samples.

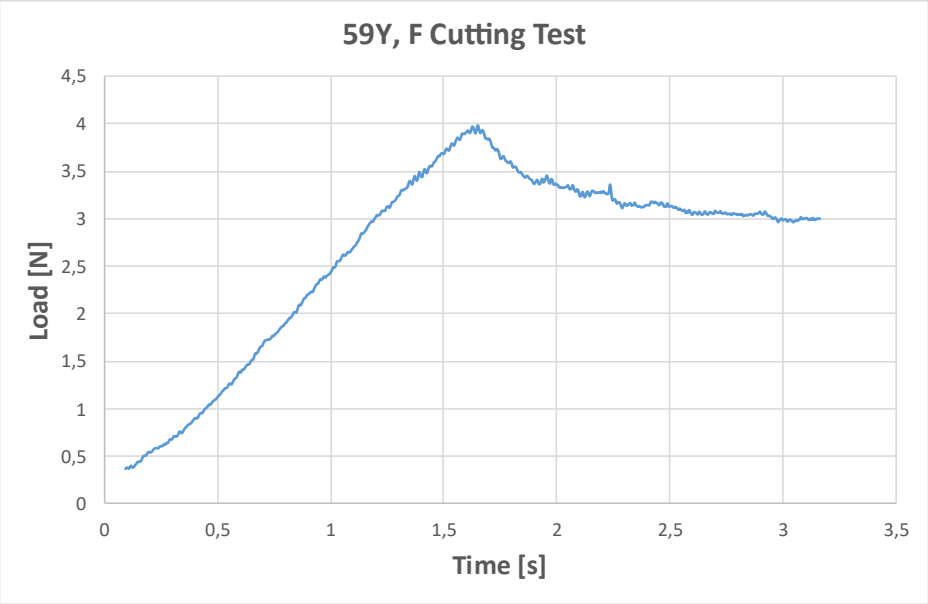


Figure 28: Result of the cutting test on the ex vivo skin sample (59Y, F only).

Table 16: Results of the cutting test on the 59Y, F sample.

		[N]
59Y, F	**Peak Force**	3,98
	Plateau Average Force	3,09

5.2 Suturable Skin DAC Presets

The research and development phase of the suturable skin presets involved the evaluation of more than 40 material mixtures. The assessment was conducted through successive rounds of testing, combining qualitative and quantitative analyses to understand and control the behavior of the different formulations. Suture traction and puncture tests were identified as the most informative methods for the initial evaluation of mechanical performance and therefore guided the overall development process. Of the more than 40 mixtures considered, 33 were characterized by at least suture, puncture, and qualitative testing.

Despite their minor differences, all presets are based on three main layers:

- an Outer Layer, 0.3 mm thick, intended to reproduce skin softness, composed of 50% Agilus and 50% Tissue Matrix for all the presets, using a "Digital Material"[1] configuration;
- an Internal Layer (Layer 2), 0.8 mm thick, designed to withstand suture traction thanks to the inclusion of a "Gyroid"[2] internal microstructure (Figure 29);
- A Background mimicking the subcutaneous fat, composed of 50% Tissue Matrix and 50% Gel Matrix for all the presets, using a "Digital Material" configuration.

An additional inner layer (Layer 3) was included between the internal layer and the background in Preset #4, to enhance adhesion between the skin and the subcutaneous fat.

Achieving realistic softness and resistance to suturing involves two conflicting requirements: therefore, identifying a suitable trade-off between these parameters was critical to obtain a clinically applicable solution.

In the following, the four final mixtures (#1, #2, #3 and #4) are presented.

[1] "Digital Material" configuration refers to a random distribution of droplets of the selected materials according to the defined percentages.

[2] "Gyroid" microstructure is defined by a "Scale" parameter which sets the gyroid cell dimensions, equal along the three axes, and a "Ratio" parameter, which controls the thickness of the gyroid walls. A base material or a custom-defined material can be selected for both the gyroid walls and the gyroid background.

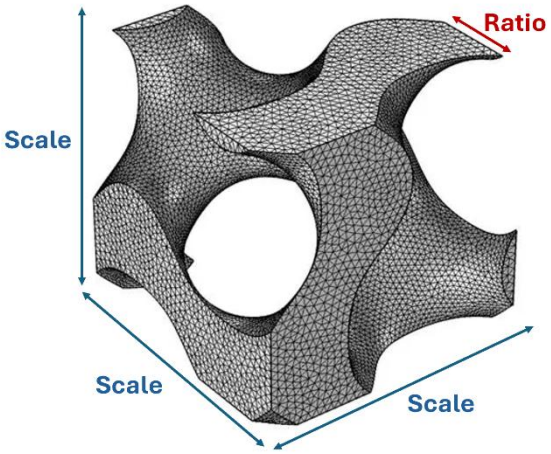


Figure 29: Gyroid structure and control parameters. "Scale" parameter controls the size of the gyroid cell, while "Ratio" controls the thickness of the gyroid cell walls.

Preset #1

The internal layer consists of a gyroid microstructure, where the gyroid is composed of 60% Bone Matrix and 40% Agilus, and the gyroid background is composed of 95% Agilus and 5% Gel Matrix. The gyroid architecture is controlled by the gyroid to background ratio, which tunes the thickness of the gyroid structure, set to 75- 25 (gyroid versus background), and by the scale factor, which tunes the size of the gyroid cell, set to 0.75. Cell orientation is controlled through the rotation parameter, set to 45° for all presets.

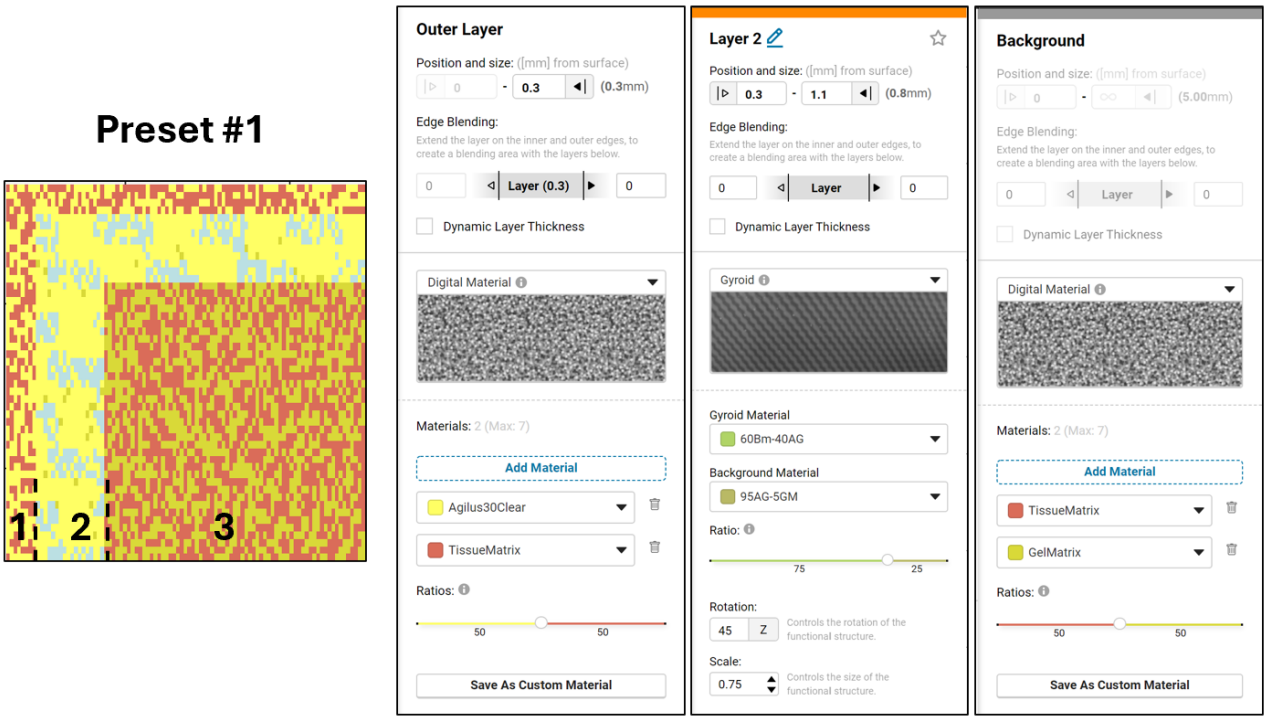


Figure 30: Detail of Preset #1 composition, with a view of the DAC windows for each layer.

Preset #2

The internal layer features the same structure as Preset #1. The only difference concerns the composition of the gyroid background, which is 90% Agilus and 10% Gel Matrix. The additional 5% Gel Matrix reduces the contribution of the background to stitch resistance, making this preset more suitable for softer tissues with low resistance to suturing.

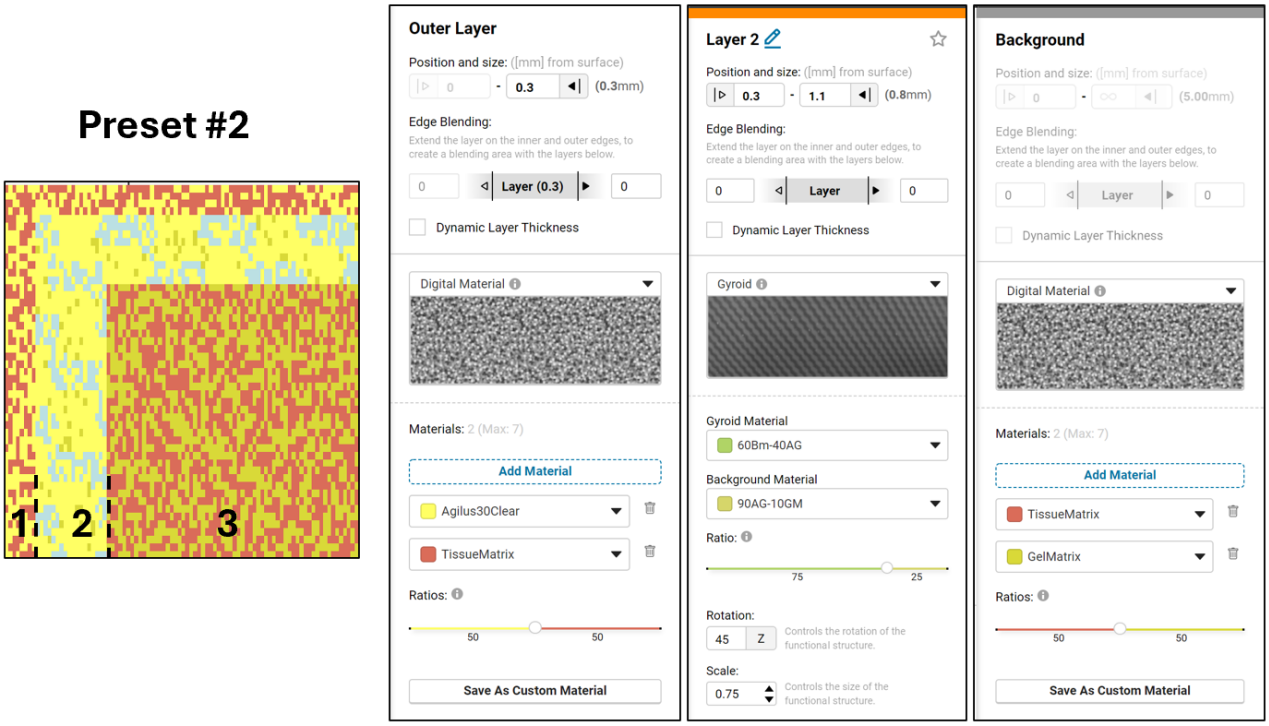


Figure 31: Detail of Preset #2 composition, with a view of the DAC windows for each layer.

Preset #3

Preset #3 also follows the same structure as Preset #1. The composition of the gyroid and gyroid background remains unchanged, while the scale factor is increased from 0,75 to 1,0. While maintaining a comparable resistance to suturing, the larger cell size provides a softer feel and increased elasticity, making this preset more suitable for tissues that are stiffer yet retain good suture resistance.

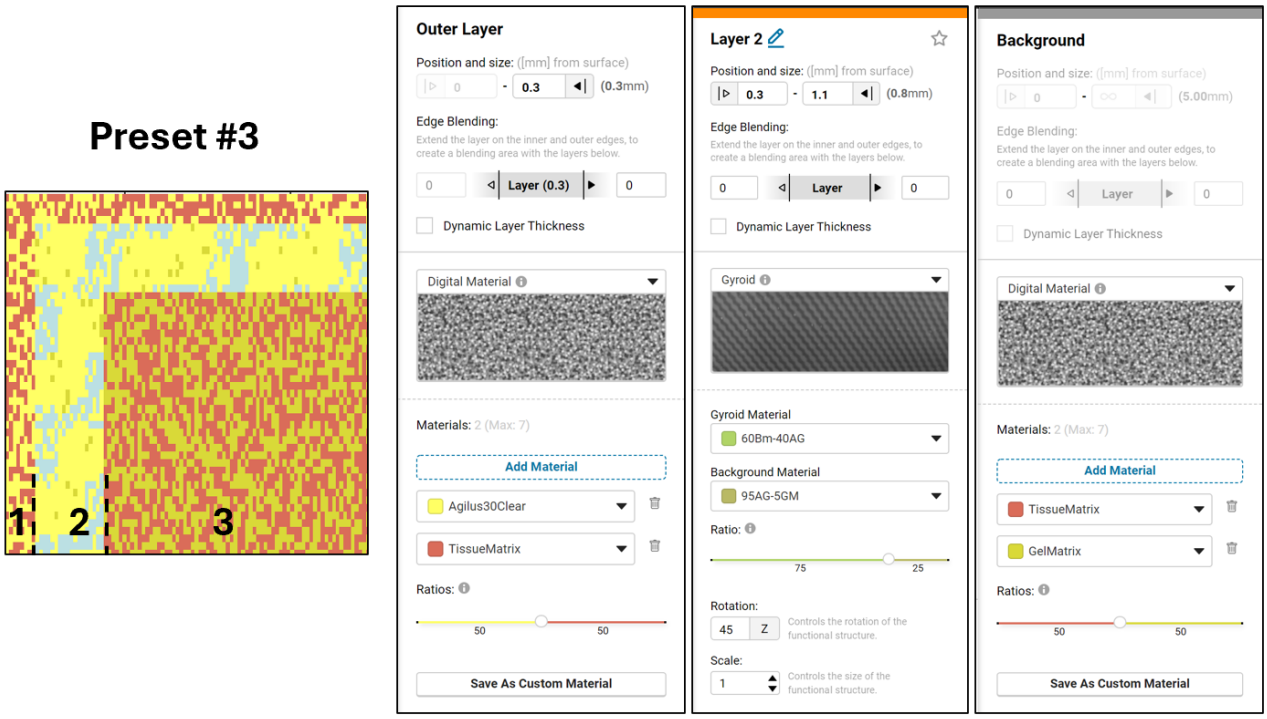


Figure 32: Detail of Preset #3 composition, with a view of the DAC windows for each layer.

Preset #4

Although similar to the previous presets in terms of overall structure, Preset #4 includes an additional layer between the internal layer and the background to improve adhesion. The internal layer is 0.8 mm thick, as in the other presets, and features a gyroid structure composed of 70% Bone Matrix and 30% Agilus, resulting in a stiffer gyroid than in Presets #1, #2 and #3. Conversely, the gyroid background is composed of 85% Agilus and 15% Gel Matrix, thus softer than in the previous mixtures. The gyroid-to-background ratio is kept at 75%-25%, and the scale factor is set to 0.8, slightly higher than in Presets #1 and #2. The larger cell size, combined with a softer gyroid background, provides an overall more realistic feel.

The additional layer is 0.3 mm thick and is a digital material composed of 85% Agilus and 15% Gel Matrix. This layer serves two purposes: it increases the overall thickness of the skin layer, compensating for the softer gyroid background, which has been shown to contribute to suture resistance, and it enhances adhesion between the skin and the subcutaneous fat, resulting in more realistic behavior during skin retraction.

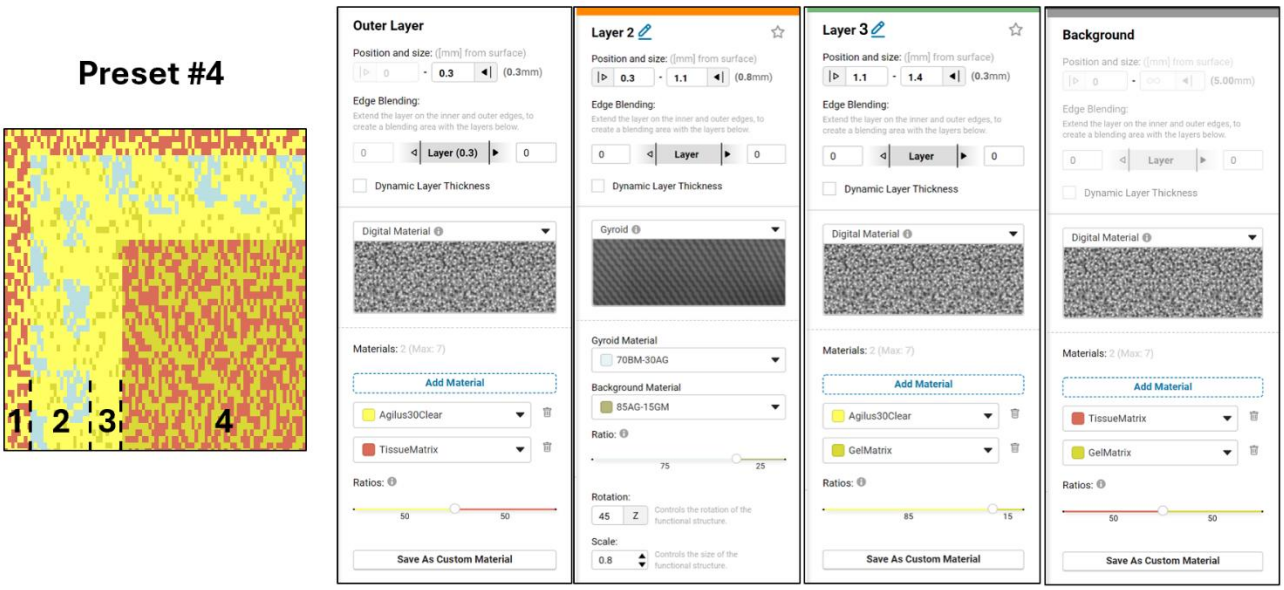


Figure 33: Detail of Preset #4 composition, with a view of the DAC windows for each layer.

The main differences in the internal layer, which is designed to withstand suture traction, are reported in Table 17. Based on the droplet distribution, a 75:25 ratio corresponds to a gyroid wall thickness of approximately 0.45 mm.

Table 17: Composition of the internal layer for the four Presets. BM = Bone Matrix, AG = Agilus, GM = GelMatrix.

	Gyroid		Gyroid Background		Ratio	Scale
	BM [%]	AG [%]	AG [%]	GM [%]		
Preset #1	60	40	95	5	75-25	0,75
Preset #2	60	40	90	10	75-25	0,75
Preset #3	60	40	95	5	75-25	1
Preset #4	70	30	85	15	75-25	0,8

5.3 Suturable Skin Presets Mechanical Properties

In the following, the results of the mechanical tests performed on the four final Presets are reported. Puncture and suture traction tests were carried out on samples printed with both the Stratasys J750 and the J5 Digital Anatomy® printers, whereas cutting and peeling tests were performed only on samples printed with the Stratasys J750. Where available, results are presented in comparison with the ex vivo skin test results.

Table 18: Results of the puncture and suture traction tests on the 3D-printed samples and ex vivo skin samples.

Material Preset		Single Stitch Traction Test						Puncture Test		
Name	Sample Thickness [mm]		Peak Force [N]	Ultimate Stress [N/mm^2]	Max Displacement [mm]	Max Displacement Norm [1/mm]	# Samples		Unit Peak Force [N/mm]	# Samples
#1 - J750	1,1	MEAN	5,97	23,61	5,05	1,47	10	MEAN	1,20	10
		SD	0,50	1,97	0,74	0,21		SD	0,18	
		RSD%	8,34%	8,34%	14,68%	14,12%		RSD%	15,02%	
#1 - J5	1,1	MEAN	7,16	28,30	5,55	1,68	10	MEAN	1,60	10
		SD	1,04	4,10	1,07	0,34		SD	0,27	
		RSD%	14,50%	14,50%	19,31%	20,12%		RSD%	16,67%	
#2 - J750	1,1	MEAN	5,79	22,88	5,23	1,54	10	MEAN	0,93	10
		SD	0,64	2,54	1,12	0,37		SD	0,19	
		RSD%	11,12%	11,12%	21,48%	23,87%		RSD%	20,69%	
#2 - J5	1,1	MEAN	5,47	21,64	4,84	1,46	10	MEAN	1,10	9
		SD	0,99	3,93	0,93	0,26		SD	0,17	
		RSD%	18,16%	18,16%	19,23%	17,48%		RSD%	15,08%	
#3 - J750	1,1	MEAN	6,65	26,27	4,98	1,44	8	MEAN	1,18	10
		SD	0,32	1,27	0,75	0,29		SD	0,24	
		RSD%	4,84%	4,84%	15,14%	19,83%		RSD%	19,98%	
#3 - J5	1,1	MEAN	7,53	29,76	6,24	1,74	10	MEAN	1,51	10
		SD	0,99	3,91	1,56	0,40		SD	0,40	
		RSD%	13,15%	13,15%	24,93%	23,02%		RSD%	26,69%	
#4 - J750	1,4	MEAN	6,31	19,59	5,15	1,17	8	MEAN	0,86	9
		SD	0,51	1,59	0,78	0,18		SD	0,17	
		RSD%	8,09%	8,09%	15,05%	15,32%		RSD%	19,89%	
#4 - J5	1,4	MEAN	6,62	26,15	5,29	1,57	8	MEAN	0,89	9
		SD	0,71	2,81	0,94	0,29		SD	0,21	
		RSD%	10,76%	10,76%	17,74%	18,39%		RSD%	23,16%	
31Y, F	3,1	MEAN	35,21	49,38	7,59	0,80	3	MEAN	0,71	5
		SD	8,10	11,36	1,63	0,27		SD	0,34	
		RSD%	23,01%	23,01%	21,49%	33,32%		RSD%	47,13%	
59Y, F	1,4	MEAN	27,08	73,13	7,91	1,95	6	MEAN	1,07	12
		SD	4,64	14,04	2,36	0,60		SD	0,33	
		RSD%	17,12%	19,20%	29,88%	30,73%		RSD%	31,12%	

5 Results of Mechanical Tests

5.4.1 Puncture Test

Results show that all presets printed with the J750 fall within the physiological range obtained from the ex vivo puncture tests, with Unit Peak Force during puncture increasing with age. Only Presets #1 and #3 printed with the J5 are slightly above this range.

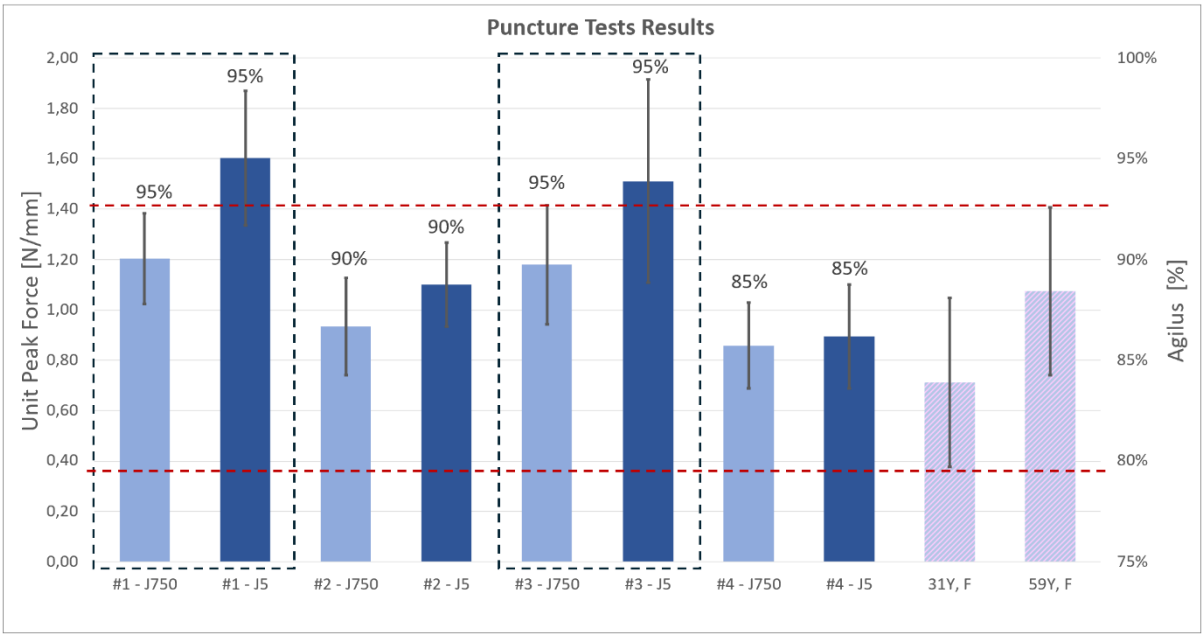


Figure 34: Results of puncture tests. The red dotted lines indicate the physiological range of values stratified by age.

Presets #1 and #3 exhibit higher puncture forces than Presets #2 and #4, and are therefore more suitable for simulating stiffer skin regions. Conversely, Presets #2 and #4 are intended to represent softer regions. For all presets, puncture tests show a trend toward higher values when printed with the J5 compared with the J750. This effect appears more pronounced with increasing Agilus content in the mixture. Agilus is the stiffest material among those used for the gyroid background and for the other digital materials in the outer layer or background.

Within the internal layer, the gyroid background is the component that contributes most to the puncture peak force. In fact, it is statistically less likely for the needle to puncture directly through the gyroid walls, which are very thin. This is further supported by the slightly lower puncture peak force measured in Preset #3 compared with Preset #1. Preset #3 features a gyroid cell scale of 1.0, whereas Preset #1 has a scale of 0.75. As the scale increases, the relative contribution of the background increases with respect to the gyroid walls. In any

case, the presence of the microstructure increases variability compared with homogeneous digital materials. Data were computed from 9 to 10 valid repetitions for each configuration (see Table 18).

5.4.2 Suture Traction Test

Resistance to suture traction remains one of the most challenging targets to meet. As mentioned in Section 5.1.3, the reference values computed for the ex vivo skin samples correspond to suture filament rupture, not to rupture of the skin specimen. Human skin has a high resistance to tearing, whereas soft photopolymers can be easily torn by the action of a thin filament. Moreover, the thinner the filament, the lower the measured resistance to suture traction [33]. In clinical practice, sutures smaller than 3-0 are not used for skin closure. Even if a smaller filament were adopted, rupture would be expected to occur at even lower forces. In Figure 35, the yellow dotted line indicates the minimum filament rupture force recorded during testing, which can be used as a reference threshold to interpret results obtained on the 3D-printed samples.

Unlike the puncture test, where the gyroid background largely governed the peak force, suture traction depends on a combination of parameters, including gyroid wall composition (expressed as Bone Matrix versus Agilus content), gyroid background composition (expressed as Agilus versus Gel Matrix content) and gyroid cell size. These three parameters are reported in Figure 35 to provide an overview of the results.

Preset #1 and Preset #2 share the same gyroid wall composition and cell size but differ in the gyroid background formulation. Preset #2 includes a higher fraction of Gel Matrix, 10% instead of 5%, and shows slightly lower peak forces than Preset #1, supporting the sensitivity of suture traction to the gyroid background composition.

Preset #3 retains the same material composition as Preset #1, while the scale factor is increased, resulting in a larger cell size. The two configurations show comparable behavior, with slightly higher values for Preset #3. This can be explained by the increased proportion of gyroid background relative to the gyroid walls, at the same wall thickness, which increases the overall contribution of Agilus within the internal layer.

Based on puncture testing, higher Agilus fractions are associated with higher peak forces, and therefore with stiffer tissue behavior. To simulate softer skin, the Agilus content in the gyroid background should be reduced, while maintaining adequate resistance to suture traction by stiffening the gyroid walls. In Preset #4, the reduction of Agilus in the gyroid background to 85% is compensated by increasing Bone Matrix in the gyroid walls to 70%. Importantly, Preset #4 also includes an additional 0.3 mm layer that effectively extends the same 85% Agilus and 15% Gel Matrix composition, increasing the overall thickness of the compliant region.

Also for the suture traction tests, the presence of the microstructure increases variability compared with homogeneous digital materials. Data were computed from 8 to 10 valid repetitions for each configuration (see Table 18).

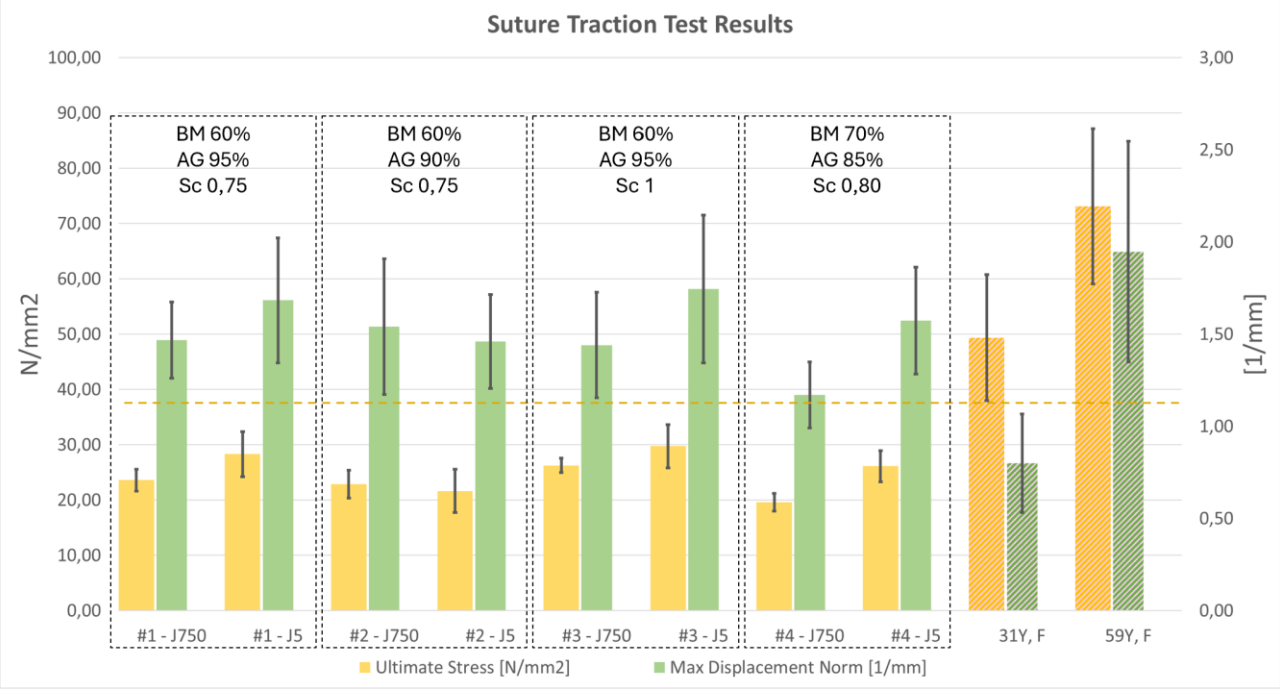


Figure 35: Results of the suture traction tests. The yellow dotted line indicates the minimum suture filament rupture force recorded during tests on ex vivo skin samples.

5.4.3 Cutting Test

The cutting test was performed only on samples printed with the Stratasys J750. As expected, all Presets showed higher cutting force values than ex vivo skin, ranging from 10.32 N to 12.78 N, compared with the 3.98 N peak cutting force recorded for ex vivo skin (Table 19). Differences were also observed in the force profile (Figure 36, Figure 37). In ex

vivo skin, the cutting force typically reaches a plateau after the initial peak. In all four Presets, instead, the force drops after the initial peak and then increases again with an oscillatory pattern. This behavior is attributed to the ease with which the photopolymer tears: once cutting starts, a portion of material distal to the blade begins to tear, reducing sliding resistance, then, as the blade engages a new intact region, the force increases again. Curve 4_C is likely representative of an incomplete blade insertion, which affected only the outermost skin layer and resulted in lower peak and sliding forces. The curve is shown in the graph but was excluded from the calculations (Table 19). The peak value used for comparison refers to the maximum reached during the initial phase of the curve, before the subsequent decrease, even though the secondary increase may reach values higher than the first peak.

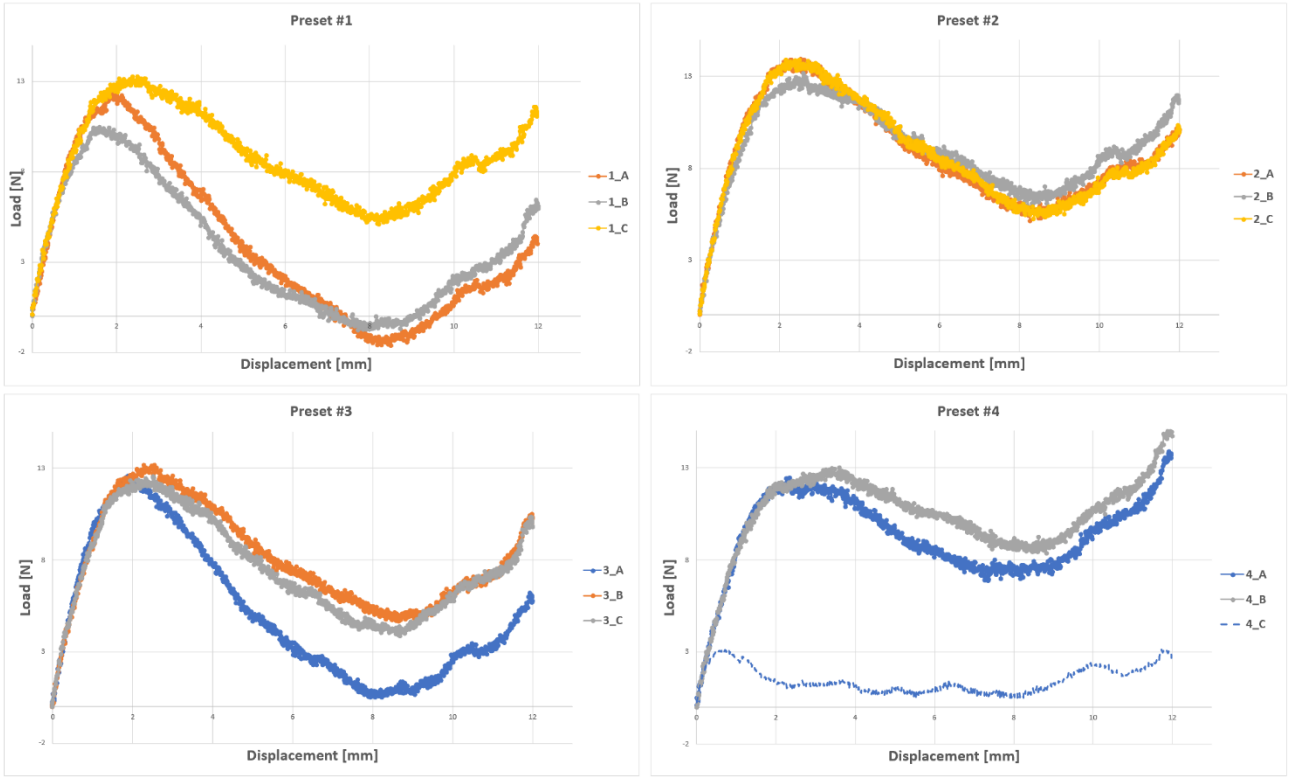


Figure 36: Results of the cutting tests on the four Presets. Curve 4_C is representative of an incorrect blade insertion, and it is excluded from calculations.

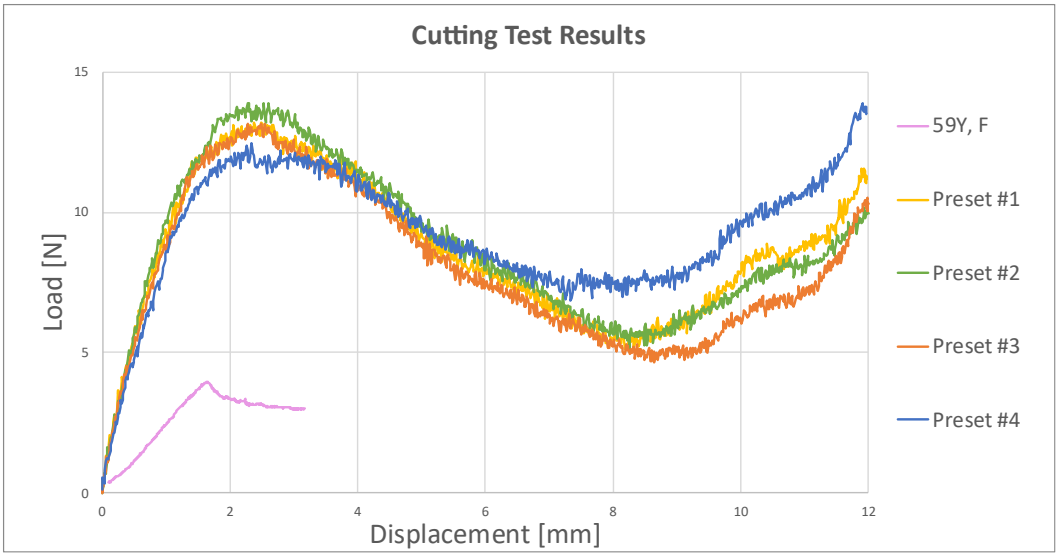


Figure 37: Comparison of a single representative curve for each Preset with the ex vivo skin sample (59Y, F).

Qualitative observations suggest that moisturizing the material with a 15% glycerol-in-water solution, used as the final step of the cleaning process, immediately before use, can reduce the cutting force. The cutting test was conducted only on the final samples, as can be correlated with suture traction force. Configurations tested during Presets' development that exhibited higher Ultimate Stress values with respect to the four final ones were also qualitatively assessed as too stiff to cut.

Table 19: Peak cutting force values recorded during cutting tests.

		Peak Force [N]	# Sample
Preset #1	MEAN	**11,39**	3
	SD	1,64	
	RSD%	14,43%	
Preset #2	MEAN	**12,62**	3
	SD	2,10	
	RSD%	16,64%	
Preset #3	MEAN	**12,78**	3
	SD	0,35	
	RSD%	2,76%	
Preset #4	MEAN	**12,74**	2
	SD	0,39	
	RSD%	3,09%	
59Y, F		**3,98**	1

5.4.4 Peeling Test

The peeling test was performed only on samples printed with the Stratasys J750. Presets #1, #2, and #3 showed very similar peeling forces, approximately 0.6 N. This extremely low value is consistent with the surgeons' feedback, particularly for the abdominal surgery case, indicating insufficient adhesion between the skin and the subcutaneous fat, which was considered unrealistic for younger patients.

Preset #4 includes an additional intermediate layer specifically introduced to address this limitation. Accordingly, the peeling force approximately doubled for Preset #4, confirming the effectiveness of the added layer in improving adhesion between the inner skin layer and the subcutaneous fat.

Compared with the other samples, these results also highlight the need for dry cleaning of peeling specimens, to avoid compromising the internal structure, which cannot be isolated from the external surfaces.

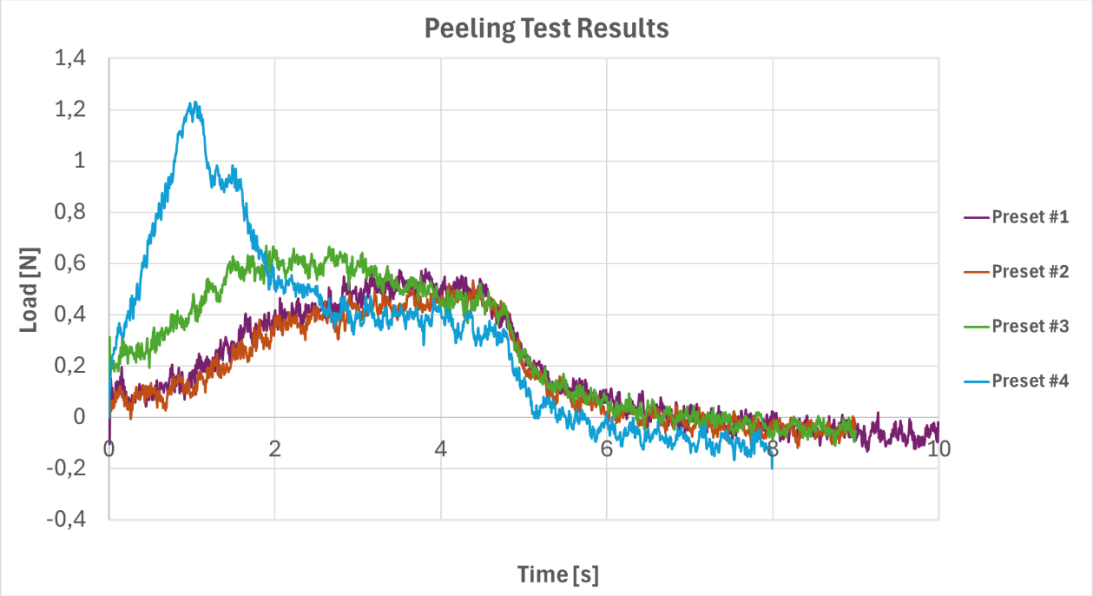


Figure 38: Results of the peeling tests on the four Presets.

Table 20: Peak peeling force values recorded during cutting tests.

Sample	Peak Force [N]
Preset #1	0,58
Preset #2	0,53
Preset #3	0,67
Preset #4	1,23

5.5 Suturable Skin Presets Qualitative Results

Mechanical characterization results were combined at each testing round with qualitative outcomes obtained through evaluations performed by expert surgeons from the two target disciplines, oto-neurosurgery and laparoscopic abdominal surgery. Notably, the differences among the final Presets are minimal. Nevertheless, surgeons were able to consistently discriminate among them and to describe their distinctive behavior. Based on their feedback, the four Presets were assigned to anatomical sites.

Three main anatomical regions were considered:

- the abdomen;
- the back, arms and legs;
- the head and neck.

For the abdomen and the back, arms and legs, further stratification by age was adopted. For the head and neck, a more general distinction between softer and tougher skin was proposed because, particularly in the temporal region, patient age typically has limited impact on suturing technique. For simplicity, these are referred to as “young” and “old”, intended as tougher skin for younger patients and softer skin for older patients.

- Abdomen, young: Preset #4
- Abdomen, old: Preset #2

- Back, arms and legs, young: Preset #3
- Back, arms and legs, old: Preset #1

- Head and neck, young (tough): Preset #4
- Head and neck, old (soft): Preset #2

Qualitative evaluations and anatomical attributions are consistent with the mechanical test results. Preset #2 and Preset #4 were selected for softer regions such as the abdomen and the head and neck. They feature a lower Agilus content, which was associated with lower puncture forces. Between these two, Preset #4 was assigned to younger or tougher skin because it provides a more favorable balance between softness, enabled by the reduced Agilus content, and resistance to suturing, supported by the additional layer and the increased Bone Matrix fraction in the gyroid walls.

Preset #1 and Preset #3 were selected to mimic stiffer anatomical sites such as the back, arms and legs. They include a higher Agilus content in the gyroid background, which is associated with higher puncture forces and improved resistance to suture traction. Preset #3, in particular, was assigned to younger skin types due to the larger gyroid cell size, which increases the relative contribution of the background over the gyroid walls and reduces puncture force.

Although a representative geometry was used for qualitative testing, final validation was performed on a patient-specific model, as presented in the following chapter.

6 Discussion and Applicative Use Cases

A final validation of the developed skin Presets was conducted on realistic anatomies to simulate two specific surgical training procedures in oto-neurosurgery and laparoscopic abdominal surgery. Expert surgeons from the two disciplines tested the procedures on the phantoms presented below.

6.1 Oto-neurosurgery of the Temporal Bone

The phantom is designed to reproduce the temporal bone with high anatomical fidelity for the simulation of drilling procedures. The model includes an outer skin layer overlying the bone, allowing trainees to practice the initial surgical steps before proceeding to the drilling phase: skin incision, soft-tissue elevation, and exposure of the underlying osseous surface. The external structure with transparent skin is shown in Figure 39. The result presented in the following is created using the “Tough/Young Head&Neck” preset (Preset #4) for the skin. The subcutaneous fat and muscle layers were printed using the same material assignments and layer thicknesses adopted during qualitative testing.

Underneath the skin layer, a series of structures, shown in Figure 40, enable the drilling of the bone. The structure includes both the cortical bone layer and the underlying trabecular network, allowing realistic feedback of drilling resistance and tactile sensations. Internally, the model incorporates the complete ossicular chain and its tendons, along with cavities for the cochlea and semicircular canals. The model also incorporates the facial nerve and the carotid along their intratemporal course.

To support spatial orientation during simulated procedures, the phantom integrates key anatomical landmarks such as the overlying dura mater, the sigmoid sinus, and the digastric ridge. Overall, this configuration provides a controlled platform for investigating drilling dynamics and verifying surgical approaches in a reproducible and anatomically representative context.

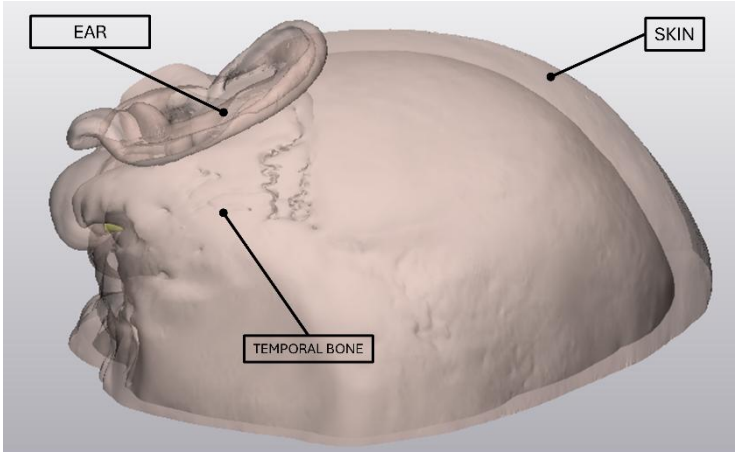


Figure 39: Exterior of the phantom with an ear and a transparent skin layer to see the underlying bone.

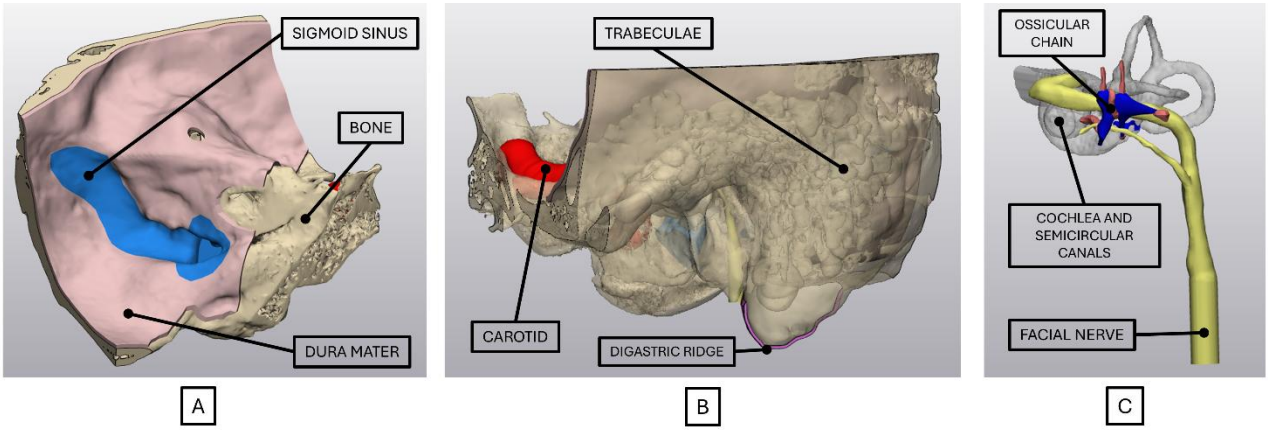


Figure 40: The temporal bone drilling phantom. (A) The sigmoid sinus and dura mater used as anatomical landmarks; (B) Temporal bone with internal trabeculae and other anatomical reference structures; (C) Details of internal structures.

Figure 41 show the skin-related steps included in the simulation: skin incision (Figure 41, step 1–2) and skin retraction (Figure 41, step 3-4), exposure of the bone (Figure 42, step 1-2), and detachment of the muscle layer from the bone (Figure 42, step 3). After completion of the surgical simulation, the skin was sutured (Figure 43). Cutting was performed using a surgical scalpel with a #10 blade, and suturing was performed using a 3-0 ETHILON* Polyamide 6 suture, 3/8 circle, 19 mm, consistent with the mechanical and qualitative tests.

All steps were successfully completed. One of the most critical steps is skin retraction to expose the bone. This maneuver is particularly demanding on the skin and can easily lead to damage in the post-auricular region. Since this area is not directly involved in cutting and suturing, it may be locally reinforced by replacing the skin Preset with pure Agilus, which provides higher tear resistance.

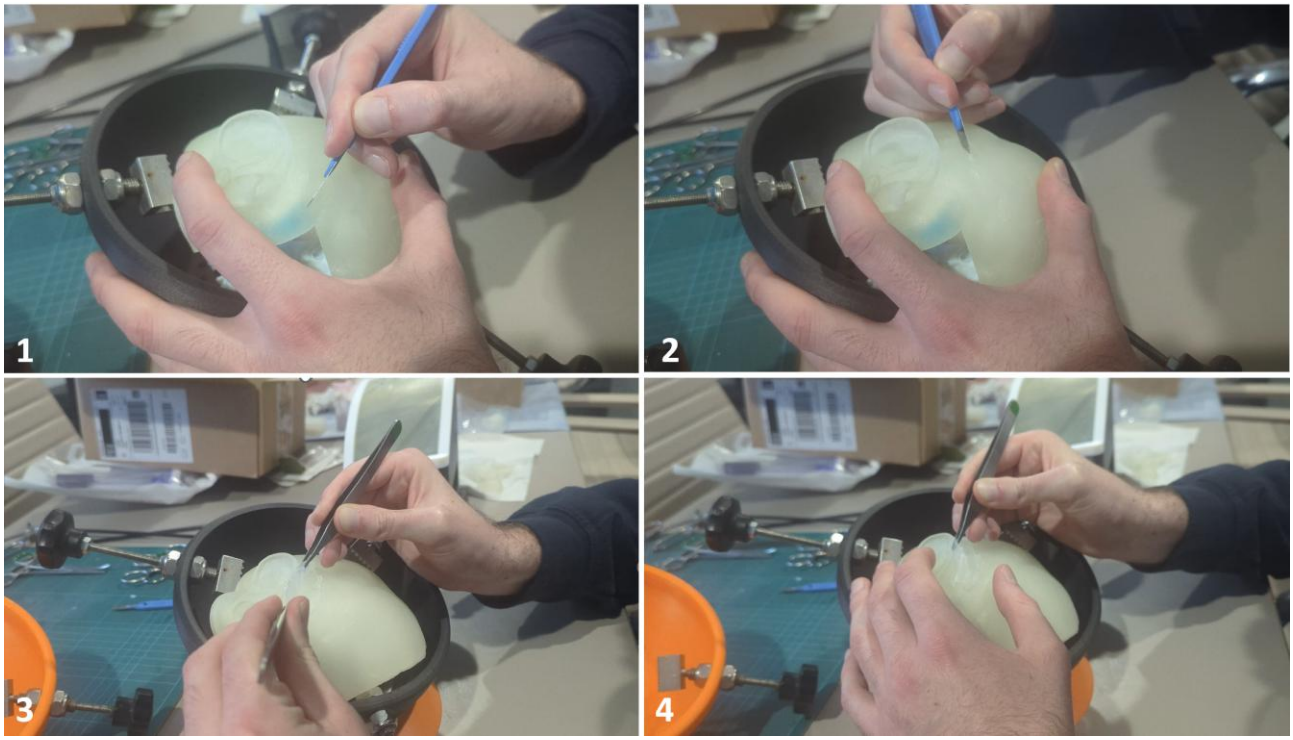


Figure 41: Skin cutting and retraction during the oto-neurosurgical procedure simulation.

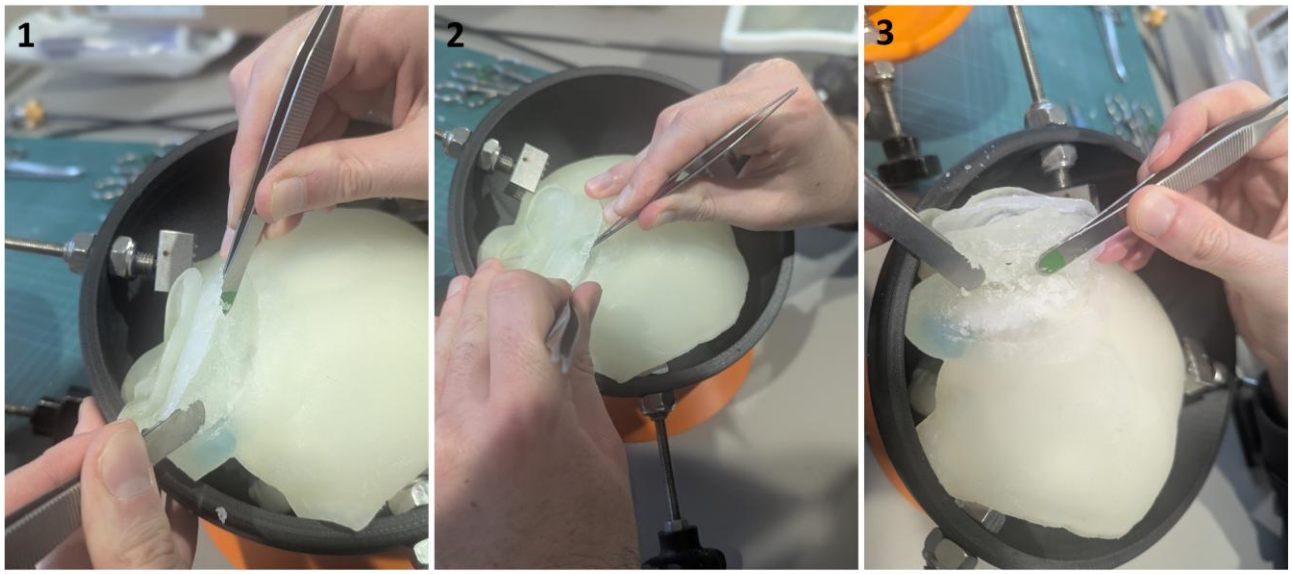


Figure 42: Skin retraction and bone exposure by detaching the muscle layer from the bone during the oto-neurosurgical procedure simulation.

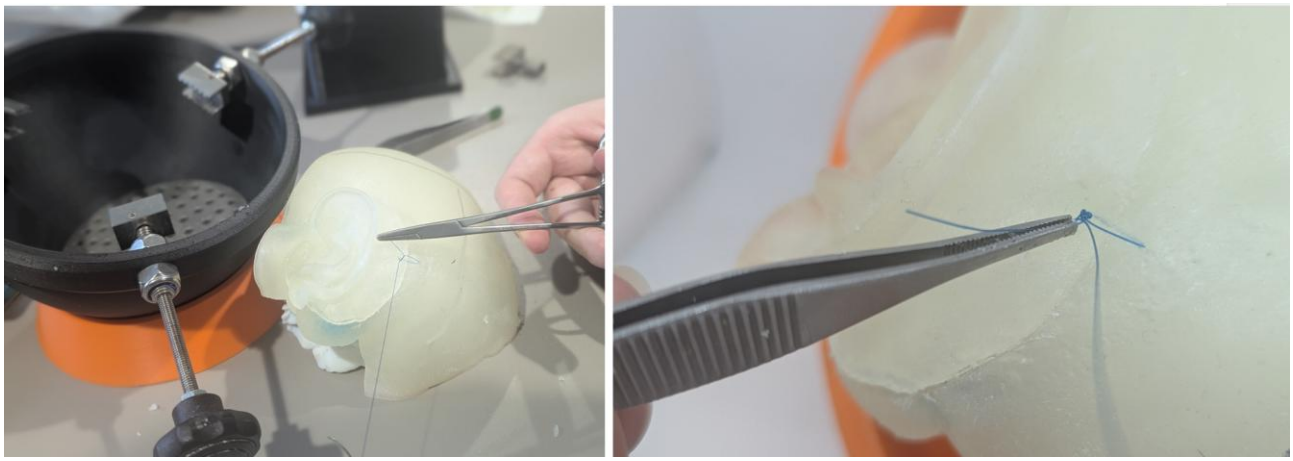


Figure 43: Skin suturing at the end of the surgical procedure.

6.2 Laparoscopic Cholecystectomy

The phantom reproduces the upper abdominal cavity, including key anatomical structures, to establish a realistic environment for laparoscopic training. It features the liver, pancreas, stomach, inferior vena cava, and portal vein to recreate the spatial relationships encountered in-vivo. Furthermore, the abdominal wall is equipped with a skin layer suitable for trocar insertion to mimic authentic access conditions. Figure 44 shows the complete anatomy included in the phantom.

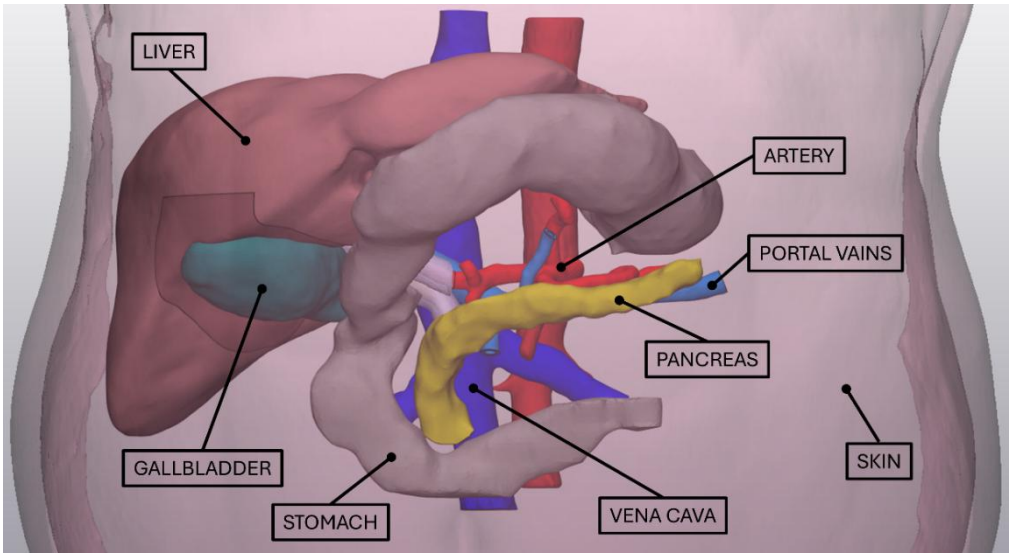


Figure 44: The anatomy of interest included in the phantom.

Within this broader anatomical environment, the model concentrates on an accurate reconstruction of the gallbladder region, where the surgical task is performed. Figure 45 focuses on the area where the surgery is performed. The hepatic artery and the cystic duct are represented along their course and branching toward the gallbladder. They are

integrated with the surrounding perivascular fat to reproduce the tissue layers that must be dissected during the procedure to expose the vessels. These elements enable trainees to practice the essential steps of cholecystectomy: isolating the arterial and ductal structures, applying clips to both the vascular branch and the cystic duct, dividing them safely, and subsequently mobilizing and removing the gallbladder from the hepatic bed. By combining comprehensive anatomical context with a detailed operative focus, the phantom offers a coherent and effective platform for developing procedural proficiency.

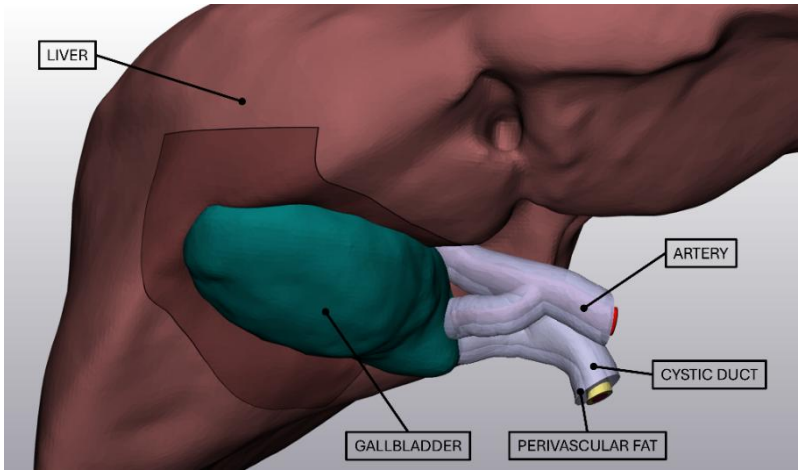


Figure 45: Detail of the surgical area

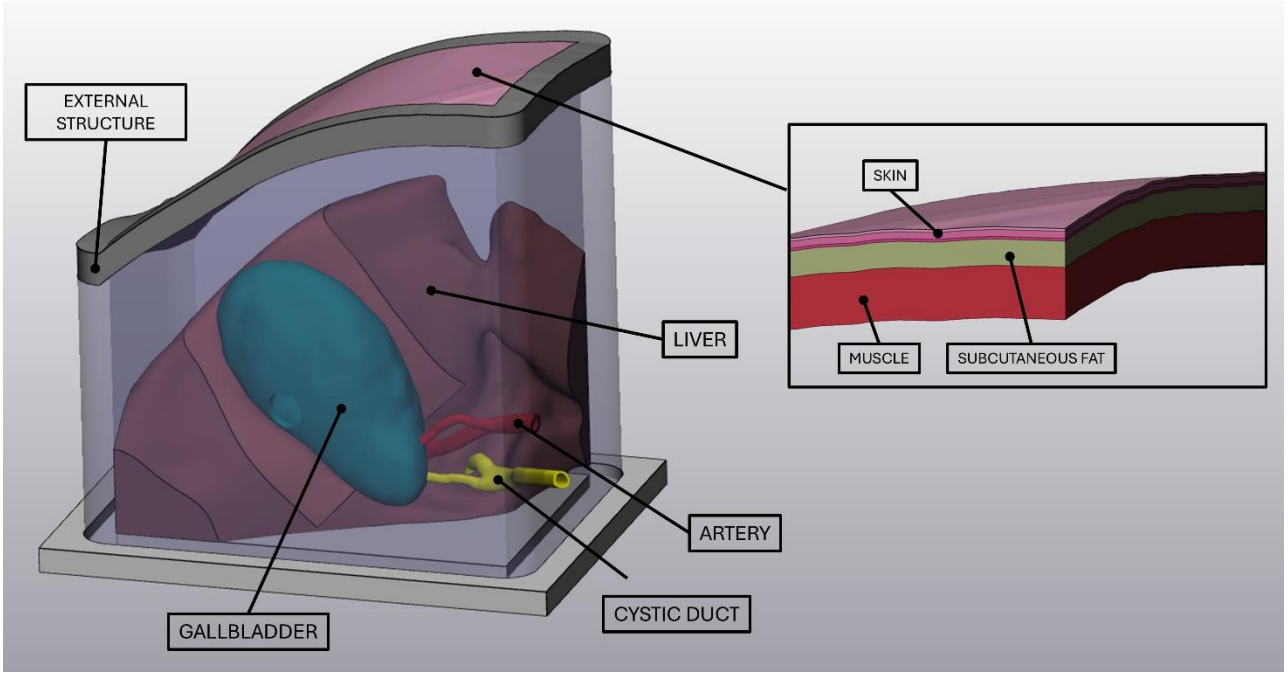


Figure 46: A simplified and smaller version of the cholecystectomy phantom designed for realistic incision and trocar insertion, for abdominal skin layer validation.

To validate the abdominal skin layer, a reduced and simplified version of the cholecystectomy phantom will be employed. This model includes only the essential internal structures related to the surgical task: the hepatic bed, the gallbladder, and the branching of the hepatic artery and cystic duct. These structures are covered by a multilayer abdominal wall designed to allow realistic incision and trocar insertion.

The result presented in the following is created using the “Young Abdomen” preset (Preset #4) for the skin while the subcutaneous fat and muscle layers were printed using the same material assignments and layer thicknesses adopted during qualitative testing. In addition to the primary access point, the reduced phantom will have dedicated openings for additional trocars and the laparoscopic camera, permitting a full range of surgical maneuvers. Figure 46 presents the reduced phantom, with a focus on the skin layer.

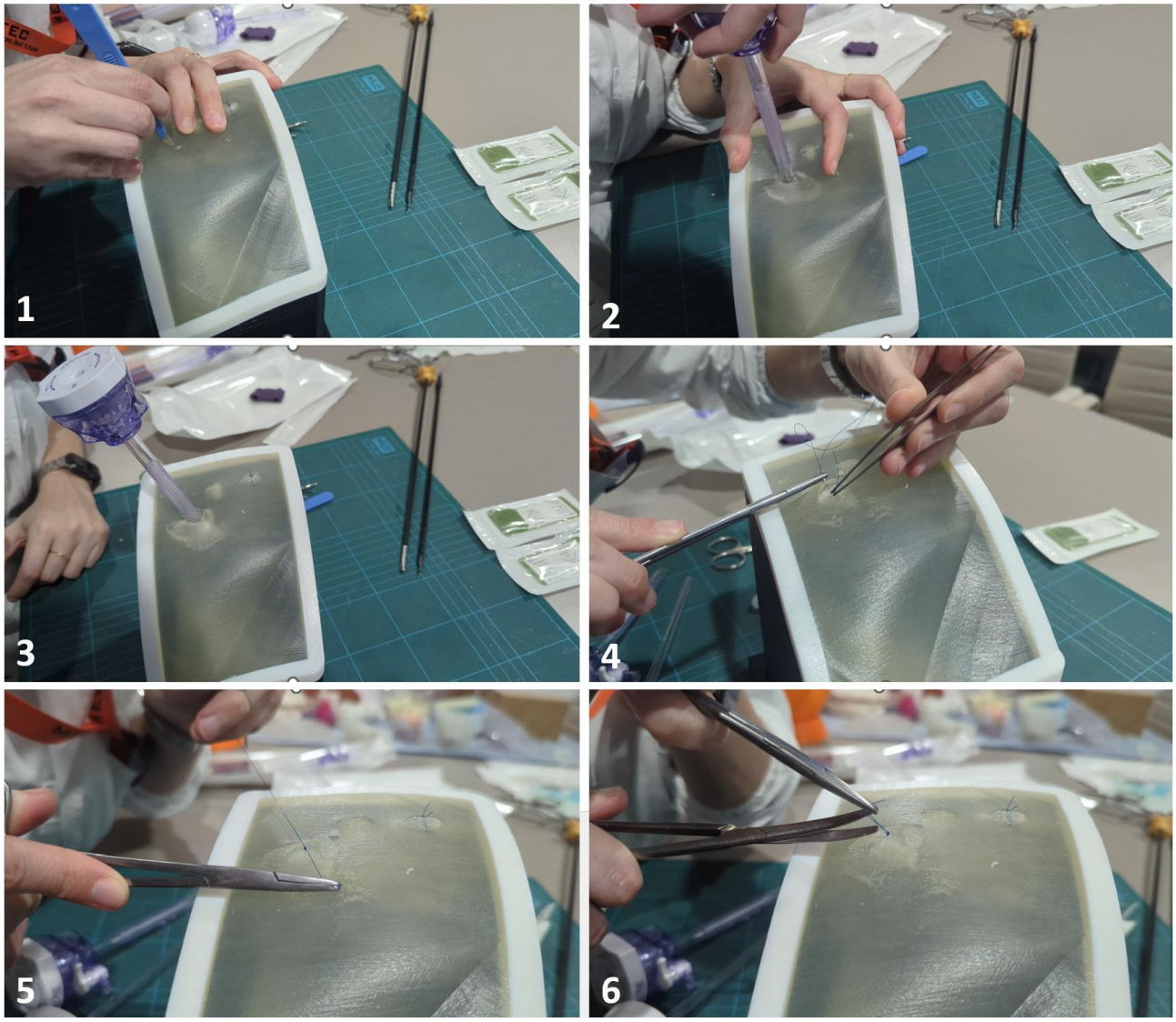


Figure 47: Steps of the surgical simulation performed on the cholecystectomy laparoscopic phantom. Skin cutting (1), trocar placement (2-3), suturing (4-5) and stitch removal (6).

The testing successfully demonstrated the simulator's ability to support all key skin-related training steps. As shown in Figure 47, the simulator enabled skin incision (Figure 47, step 1) and trocar placement (Figure 47, step 2-3). During trocar insertion, the muscle layer plays a crucial role, as it requires an additional force to be traversed by the trocar. Once the abdominal cavity is reached, the force feedback decreases. This transition was correctly reproduced by the proposed skin configuration.

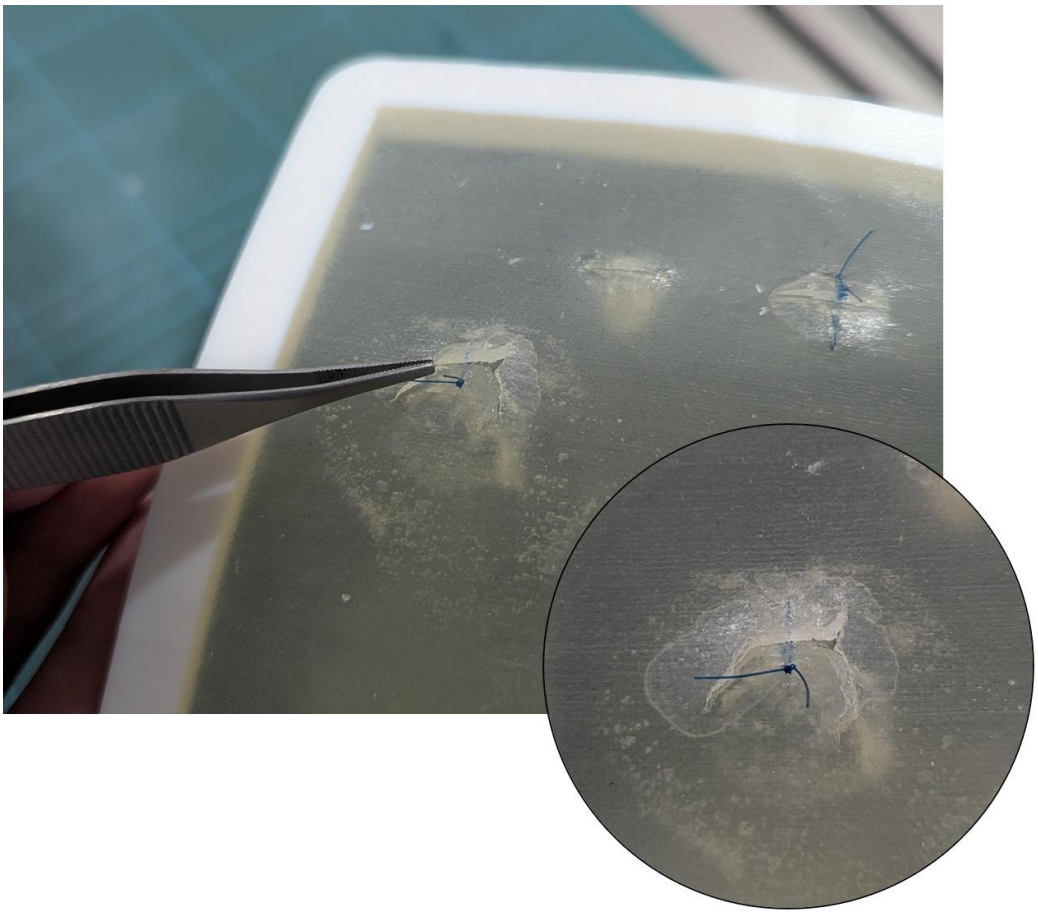


Figure 48: Detail of the stitch on the skin after trocar removal. The traumatic lesion of the trocar is visible, but the skin is still capable of holding the suture.

At the end of the procedure, the trocar was removed and the skin was sutured. As shown in (Figure 47, step 3), trocar placement is traumatic for the skin: delamination is observed, with detachment of the most superficial layer from the subcutaneous fat (Figure 48). Nevertheless, the skin remained suitable for suturing (step 4) and for securing the stitch with a realistic amount of force (Figure 47, step 5). In addition, suture traction was assessed during stitch removal, when the stitch is pulled prior to being cut (Figure 47, step 6). Cutting was performed using a surgical scalpel with a #10 blade, and suturing was performed using

a 3-0 ETHILON* Polyamide 6 suture, 3/8 circle, 19 mm, as in the mechanical and qualitative tests.

To minimize the portion of the simulator that must be replaced after each training session, the final configuration of the cholecystectomy simulator includes replaceable pads that can be inserted into a rigid skin framework (Figure 49, Figure 50, Figure 51). This approach enables faster set-up and reduces the overall cost of simulator use. The replaceable pads were tested and proved their effectiveness. The incision and trocar insertion (size #5) were performed successfully, confirming that the limited size of the realistic skin pad did not compromise the realism of the simulation. For umbilical access, two approaches were evaluated, a supraumbilical incision (Figure 52, 1-2) and a semi-circular subumbilical incision (Figure 52, 3-4). Both proved successful in terms of incision, trocar insertion, and instrument maneuverability. Skin retraction and subsequent recoil were also observed to be realistic, with the tissue returning to its original position after opening.

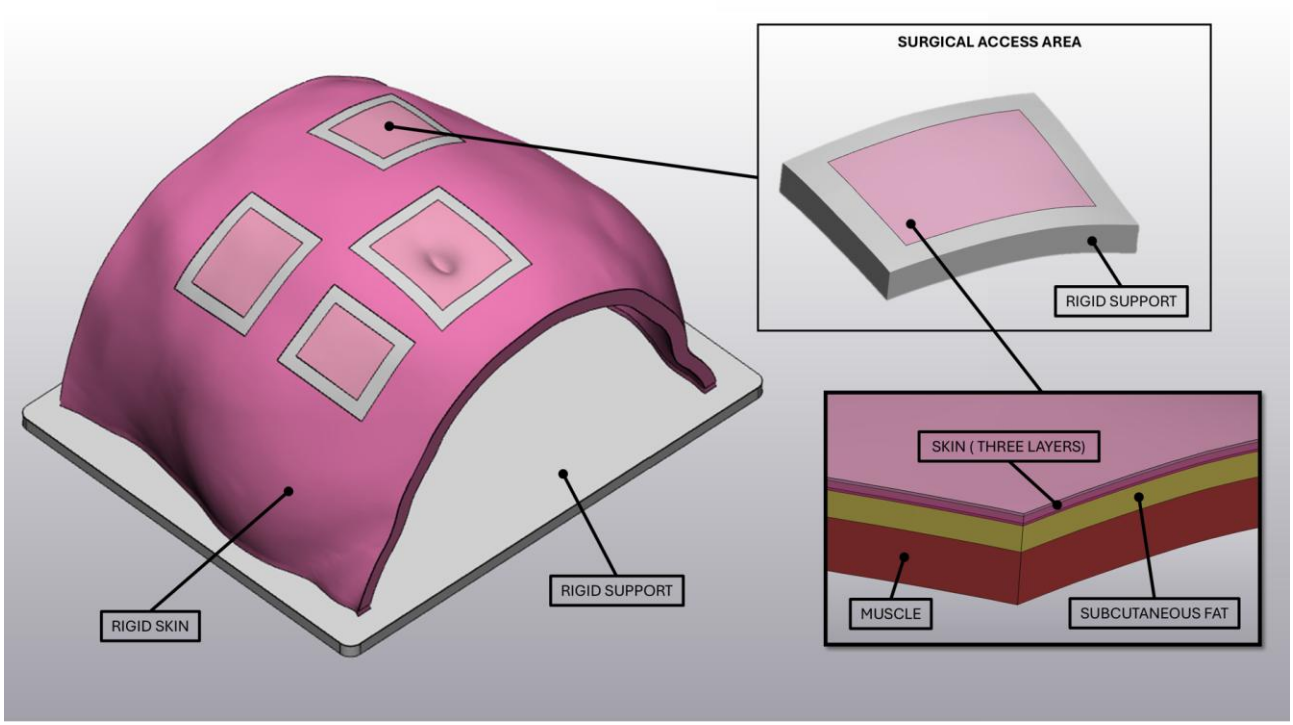


Figure 49: Overview of the laparoscopic cholecystectomy simulator. The skin is printed in a rigid material in which skin pads printed with the developed preset can be inserted and easily replaced after each simulation.

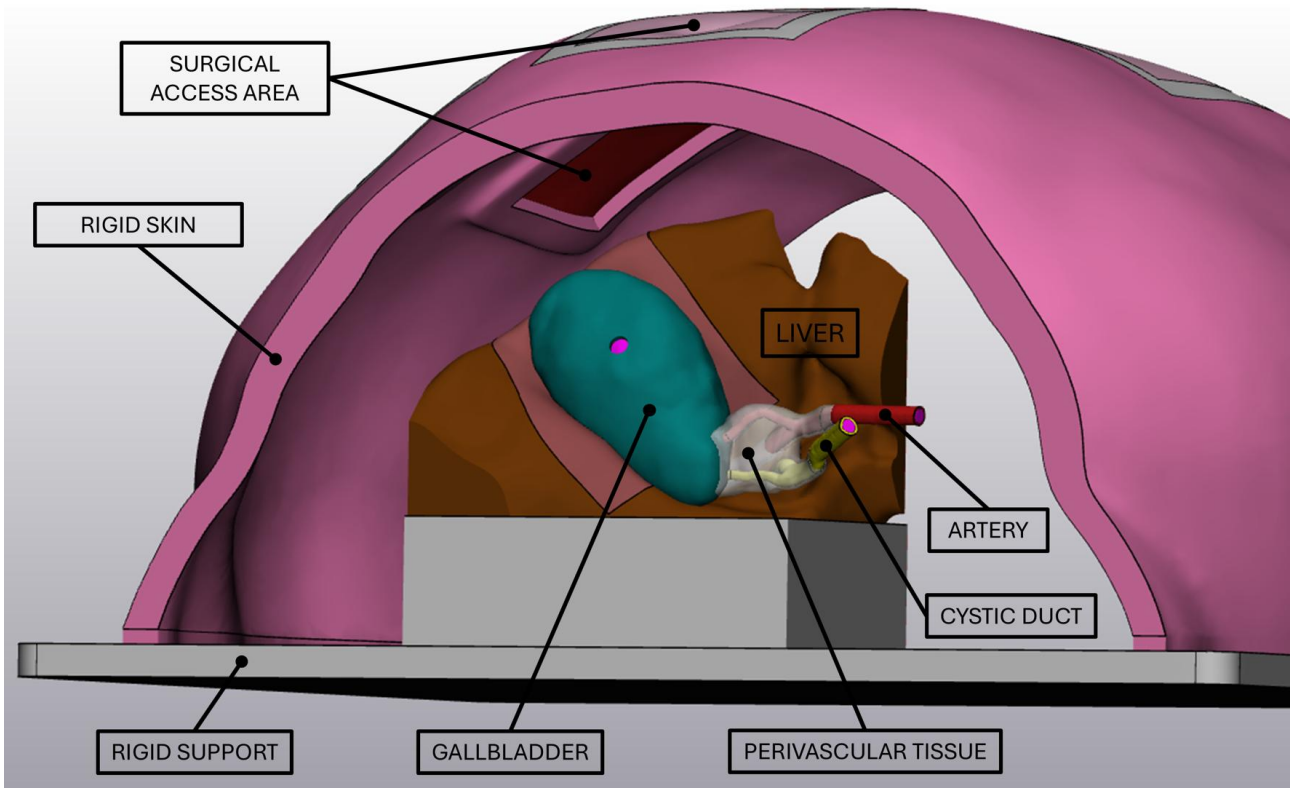


Figure 50: Inner view of the laparoscopic cholecystectomy simulator.



Figure 51: External and internal view of the 3D-printed laparoscopic cholecystectomy simulator.

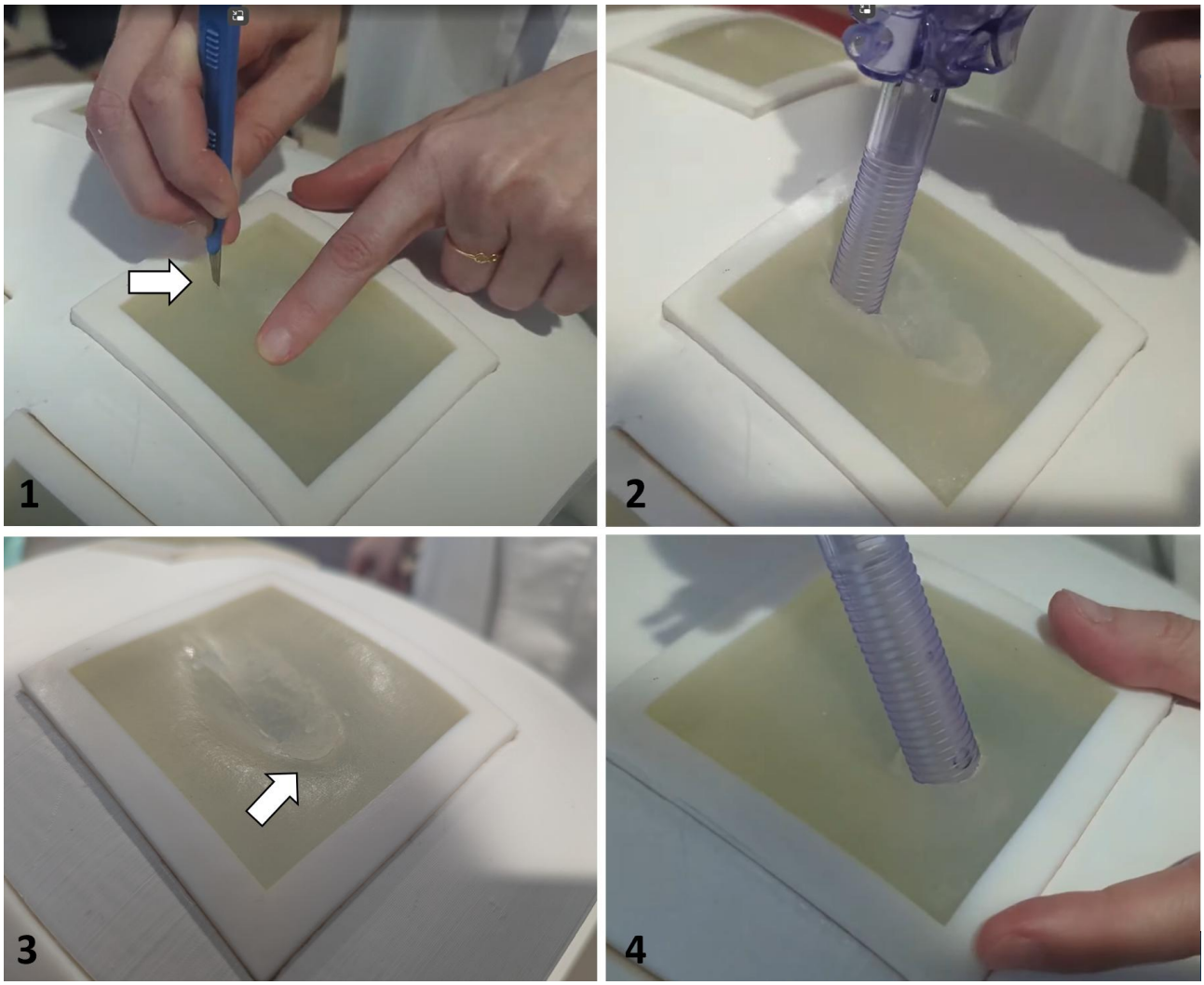


Figure 52: Umbilical incision for trocar placement: supraumbilical incision (1-2) and semi-circular subumbilical incision (3-4).

7 Conclusions

The study investigated more than 40 material Presets, together with mechanical testing of ex vivo human skin specimens. The ex vivo samples were used, on the one hand, to compare tensile test results with the literature, which provided the only directly comparable dataset, and, on the other hand, to establish a reference baseline for the suturability-related tests.

A total of 33 material Presets underwent both mechanical screening, through puncture and suture traction tests, and qualitative evaluation with the support of expert surgeons in oto-neurosurgery and laparoscopic abdominal surgery, which were selected as the two target application domains for the development.

Four final Presets were developed and fully characterized through puncture, suture traction, cutting, and peeling tests, then analyzed in comparison with the ex vivo data and with the qualitative feedback collected during surgeon testing. The mixtures were assigned to anatomical districts based on the typical softness of the corresponding regions and stratified by age. In this context, “younger” skin refers to tissue that is typically thicker and more elastic, and therefore better able to withstand suture-related loads. Conversely, “older” skin is associated with reduced thickness and increased stiffness and is more prone to suture-induced tearing.

The final Presets were also validated in two discipline-specific application cases, namely a temporal region simulator for oto-neurosurgical procedures and an abdominal simulator for laparoscopic cholecystectomy training.

Both simulations were successfully completed and proved the capability of the developed Presets of enabling the simulation and training on the two target districts.

The primary objective of the presets is to enable the effective execution of key procedural maneuvers, thereby ensuring practical and realistic training. Nevertheless, the results clearly show that printed tissue cannot reproduce all the properties of native skin, which exhibits substantially higher tensile strength and a softer response during cutting.

The main limitation reported by surgeons was an excessively hard cutting feel. This issue can be mitigated by using surface-hydrating solutions to reduce blade friction, preferably applied immediately before use. Suture resistance was sufficient to allow stitch placement

without excessive or unrealistic tearing. It should be noted, however, that further improvement in suture resistance would necessarily require an increase in microstructural stiffness and/or specimen thickness, which would be at odds with the desired softness of the material.

Overall, the developed suturable skin presets represent an effective compromise for enabling the successful execution of procedures involving skin cutting and suturing, thereby supporting realistic education and training.

References

[1] Y. Gilaberte, Anatomy and Function of the Skin, 2016 (https://doi.org/10.1016/B978-0-12-802926-8.00001-X).

[2] A. T, "Transdermal Drug Delivery System – A Review," *Future Journal of Pharmaceuticals and health sciences,* 2022 (https://doi.org/10.26452/fjphs.v3i1.340).

[3] A. Firooz, "The influence of gender and age on the thickness and echo-density of skin," *John Wiley & Sons,* 2016 (https://doi.org/10.1111/srt.12294).

[4] D. Lintzeri, "Epidermal thickness in healthy humans: a systematic," *JEADV,* 2022 (https://doi.org/10.1111/jdv.18123).

[5] J. Moller, "Epidermal Thickness at Different Body Sites: Relationship to Age, Gender, Pigmentation, Blood Content, Skin Type and Smoking Habits," *Acta Derm Venereol,* 2003 (https://doi.org/10.1080/00015550310015419).

[6] Y. Lee, "Skin thickness of Korean adults," 2002 (https://doi.org/10.1007/s00276-002-0034-5).

[7] T. Tsugita, "Positional differences and aging changes in Japanese woman epidermal thickness and corneous thickness determined by OCT (optical coherence tomography)," 2013 (https://doi.org/10.1111/srt.12021).

[8] W. Lee, Temple Augmentation. In: Safe Filler Injection Techniques. Springer, Singapore., 2022 (https://doi.org/10.1007/978-981-16-6855-5_5).

[9] M. Yildiz, "Quantitative assessment of temporal skin elasticity using shear wave elastography in pediatric cochlear implant users," 2020 (https://doi.org/10.1016/j.ijporl.2020.110257).

[10] K. Chopra, "A Comprehensive Examination of Topographic Thickness of Skin in the Human Face," 2015 (https://doi.org/10.1093/asj/sjv079).

[11] K. Jeong, "Ultrasonographic analysis of facial skin thickness in relation to age, site, sex, and body mass index," 2023 (https://doi.org/10.1111/srt.13426).

[12] F. Gatto, "Temporal and masseter muscle evaluation by MRI provides information on muscle mass and quality in acromegaly patients," 2024 (https://doi.org/10.1007/s11102-024-01422-y).

[13] KIM, "Regional Thickness of Facial Skin and Superficial Fat," 2019 (https://doi.org/10.1002/ca.23331).

[14] Y. Uehata, "Relationship of skin hardness of the temporal region to nutritional status," 2017 (https://doi.org/10.24462/jnse.4.1_49).

[15] J. Han, "Association between the Thickness or Area of the Temporal Muscle andSkeletal Muscle Mass in Bioimpedance Analysis," 2024 (https://doi.org/10.1159/000539063).

[16] A. E. Abbas, "Assessment of Anterior Abdominal Wall Layers Thickness under the influence of Age and Sex, Using Computed Tomography Imaging in Ibn-Sina Hospital, Khartoum, Sudan 2021," *Fortune Journal,* 2022 (https://www.doi.org/10.26502/acbr.50170311).

[17] P. Rk, "Anatomy of anterior abdominal wall [Slide presentation]," (https://www.slideshare.net/slideshow/anatomy-of-anterior-abdominal-wall-158910161/158910161).

[18] Jose´G.B.Derraik, "Effects of Age,Gender, BMI, and Anatomical Site on Skin Thickness in Children and Adults with Diabetes," *Plos one,* 2014 (https://doi.org/10.1371/journal.pone.0086637).

[19] D. Dong, "Study of Individual Characteristic Abdominal Wall Thickness Based on Magnetic Anchored Surgical Instruments," *Chinese Medical Journal,* 2015 (https://doi.org/10.4103/0366-6999.161360).

[20] M. Rostami, "Relations Between Lateral Abdominal Muscles Thickness, Body," *Acta Medica Iranica,* 2013 (https://www.researchgate.net/deref/http%3A%2F%2Fwww.ncbi.nlm.nih.gov%2Fpubmed%2F23585316?_tp=eyJjb250ZXh0Ijp7ImZpcnN0UGFnZSI6InB1YmxpY2F0aW9uIiwicGFnZSI6InB1YmxpY2F0aW9uIn19).

[21] N. Tahan, "Measurement of superficial and deep abdominal muscle thickness: an ultrasonography study," *Journal of Physiological Anthropology,* 2016 (https://pubmed.ncbi.nlm.nih.gov/27553830/).

[22] Rahmani, "Normal values of abdominal muscles thickness in healthy children using ultrasonography," 2018 (https://www.researchgate.net/publication/236181994_Relations_Between_Lateral_Abdominal_Muscles_Thickness_Body_Mass_Index_Waist_Circumference_and_Skin_Fold_Thickness).

[23] Özdemir, *Tomographic Assessment of Normal Abdominal Muscle Thickness Values in Adolescents,* 2025 (https://advradiology.org/pdf/advradiology/articles/AdvRadiolImaging.galenos.2024.65375/5-7.pdf).

[24] M. Ottenio, "Strain rate and anisotropy effects on the tensile failure characteristics of human skin," *Journal of the mechanical behavior of biomedical materials,* 2014 (https://doi.org/10.1016/j.jmbbm.2014.10.006).

[25] Gallagher, "Dynamic Tensile Properties of Human Skin," 2012 (http://hdl.handle.net/10197/4772).

[26] A. N. Annaidh, "Characterization of the anisotropic mechanical properties of excised human skin," *JOURNAL OF THE MECHANICAL BEHAVIOR OF BIOMEDICAL MATERIALS,* 2011 (https://doi.org/10.1016/j.jmbbm.2011.08.016).

[27] G. Boyer, "Dynamic indentation on human skin in vivo : ageing effects," *Skin Research and Technology,* 2009 (https://doi.org/10.1111/j.1600-0846.2008.00324.x).

[28] Z. H., Characterization of the mechanical properties of a dermal equivalent compared with human skin in vivo by indentation and static friction tests, 2008 (https://doi.org/10.1111/j.1600-0846.2008.00329.x).

[29] Pailler-Mattei, In vivo measurement of the elastic mechanical properties of human skin by indentation tests, 2007 (https://doi.org/10.1016/j.medengphy.2007.06.011).

[30] G. Barreiro, "Abdominal skin tensile strength in aesthetic and massive weight loss patients ant its role in ventral hernia repair," 2019 (https://doi.org/10.1186/s12893-019-0523-7).

[31] ISO/ASTM52900: 2021, "Additive manufacturing -- General principles -- Terminology," Online, 2021.

[32] F. TB, "The validity and practicality of sun-reactive skin types I through VI.," *Arch Dermatol.,* vol. 6, no. 124 (https://doi.org/10.1001/ARCHDERM.124.6.869), pp. 869-71, Jun 1988.

[33] M. Stefania, M. Valeria, N. Erika, P. Luigi, P. Andrea and A. Ferdinando, "Quantitative Assessment of 3D Printed Blood Vessels Produced with J750™ Digital Anatomy™ for Suture Simulation," *bioRxiv,* p. 2022.01.09.475308;, 2022.